Geochemistry, Geophysics, Geosystems®

AGU ADVANCING EARTH AND SPACE SCIENCES

RESEARCH ARTICLE
10.1029/2023GC010977

Key Points:

- 2-D models of mid-ocean ridge subduction using petrological-thermomechanical modeling
- Slab separation leads to the opening of a slab window and the migration of partial melts from the mid-ocean ridge to the subcontinental mantle
- Models are consistent with geological, geophysical and geochemical observations in the Chile Triple Junction

Supporting Information:

Supporting Information may be found in the online version of this article.

Correspondence to:

J. Sanhueza,
jlsanhueza@uc.cl

Citation:

Sanhueza, J., Yáñez, G., Buck, W. R., Araya Vargas, J., & Veloso, E. (2023). Ridge subduction: Unraveling the consequences linked to a slab window development beneath South America at the Chile Triple Junction. *Geochemistry, Geophysics, Geosystems*, *24*, e2023GC010977. https://doi.org/10.1029/2023GC010977

Received 30 MAR 2023
Accepted 19 AUG 2023

Author Contributions:

Conceptualization: Jorge Sanhueza, Gonzalo Yáñez, Jaime Araya Vargas
Formal analysis: Jorge Sanhueza, Gonzalo Yáñez, W. Roger Buck
Investigation: Jorge Sanhueza, Gonzalo Yáñez, W. Roger Buck, Jaime Araya Vargas
Methodology: Jorge Sanhueza, Gonzalo Yáñez
Project Administration: Eugenio Veloso

Ridge Subduction: Unraveling the Consequences Linked to a Slab Window Development Beneath South America at the Chile Triple Junction

Jorge Sanhueza[1], Gonzalo Yáñez[1], W. Roger Buck[2], Jaime Araya Vargas[3], and Eugenio Veloso[4]

[1]Departamento de Ingeniería Estructural y Geotécnica, Pontificia Universidad Católica de Chile, Santiago, Chile, [2]Lamont-Doherty Earth Observatory, Columbia University, Palisades, NY, USA, [3]Departamento de Geología, Universidad de Atacama, Copiapó, Chile, [4]Escuela de Ciencias del Mar, Pontifica Universidad Católica de Valparaíso, Valparaíso, Chile

Abstract The subduction of an active spreading center generates a clear signature in the temporal evolution of subduction zones. It disrupts the typical arc-type magmatism and intraplate seismicity, enhances the emplacement of backarc plateau lava and profoundly change the tectonics and topographic relief. These distinct observations are commonly linked to a slab window opening and mantle upwelling. The Chile Triple Junction provides the ideal setup to study the mid-ocean ridge subduction process where both sides of the spreading center continue to subduct. Here, we use 2-D numerical petrological-thermomechanical modeling to focus on transient geodynamic processes caused by mid-ocean ridge subduction. Model results show slab separation along the ridge axis with the opening of a slab window. During the opening, partial melts from the spreading center migrate toward the subcontinental mantle and high temperatures in the forearc are predicted. The temporal evolution of the modeled temperature is consistent with observed heat flow data, and with magmatism and high-temperature metamorphism recorded in Chilean forearc rocks. Such migrated partial melts might explain the low viscosity inferred and low seismic velocity anomalies imaged in the slab window beneath South America, and the common geochemical signature of the Chile Ridge, the Taitao Ophiolite and the backarc magmatism. Following slab separation, our models suggest forearc uplift and changes in the stress regime, processes which are consistent with deformation records. Summarizing, our model of the geodynamic evolution of the Chile Ridge subduction provides a consistent framework that explains diverse records of magmatism, metamorphism, deformation and mantle physical properties.

1. Introduction

The entry of a plate spreading center (or mid-ocean ridge) into a subduction zone profoundly affects the tectonics, topographic relief, magmatism, and metamorphism of the overriding plate. Modern triple junctions involving this process, such as the Mendocino triple junction, correlate with fundamental changes including a switch from compressional to extensional tectonics for the Basin and Range Province of North America (Furlong & Schwartz, 2004). Evidence of mid-ocean ridge subduction is inferred in the geological record with eight particularly clear examples through the Cenozoic (Barker et al., 1992; Kimura et al., 2019; Madsen et al., 2006; Scalabrino et al., 2009; Sisson et al., 2003). In addition, tectonic reconstructions suggest that this process is fairly common in the Pacific Basin (Iannelli et al., 2020; Seton et al., 2015).

By mid-ocean ridge subduction, we mean that an active spreading center moves into a subduction zone, where the subducting slab separates and leads to the opening of a slab window (Uyeda & Miyashiro, 1974). There are several active tectonic settings on Earth where this process takes place: The Juan the Fuca Plate along both north and south ridge flanks under North America (Thorkelson & Taylor, 1989), the Chile Ridge system under South America (DeLong & Fox, 1977), the Panama Slab window (Johnston & Thorkelson, 1997), the Antarctic Peninsula slab window (e.g., Breitsprecher & Thorkelson, 2009; Hole & Larter, 1993) and The Woodlark basin (e.g., Chadwick et al., 2009). In all these cases a slab window opens but with different tectonic implications. For instance, in Juan de Fuca case, the subduction ceases after the slab detachment, and a strike-slip fault marks the boundary between the Pacific and North American Plate (Madsen et al., 2006). In the case of the Chile Ridge subduction, both sides of the spreading center continue to subduct along with the opening of the interpreted Patagonian slab window (Breitsprecher & Thorkelson, 2009; S. C. Cande & Leslie, 1986).

Software: Jorge Sanhueza
Supervision: Gonzalo Yáñez
Validation: Gonzalo Yáñez, W. Roger Buck, Jaime Araya Vargas
Visualization: Jorge Sanhueza
Writing – original draft: Jorge Sanhueza
Writing – review & editing: Jorge Sanhueza, Gonzalo Yáñez, W. Roger Buck, Jaime Araya Vargas, Eugenio Veloso

The consequences on the overriding plate due to the slab window opening have been commonly attributed to mantle upwelling and melting after slab separation (Thorkelson, 1996). These processes have been inferred through geophysical imaging, which provides a snapshot of the present state of the upper mantle in terms of temperature and viscosity structures (Mark et al., 2022; Russo et al., 2010). Although previous numerical (Groome & Thorkelson, 2009; Wu et al., 2022) and analog (Guillaume et al., 2010, 2013) models have been carried out to explain the Patagonian slab window, a systematic study assessing the role of the asthenosphere, partial melt properties, and the overriding/subducting plate characteristics is so far missing.

In this contribution, we focus our efforts on unraveling transient geodynamic processes using the Chile Triple Junction (CTJ) as a case study (Figure 1) which is affected by recent and ongoing mid-ocean ridge subduction of the Chile Ridge system (Breitsprecher & Thorkelson, 2009; S. C. Cande & Leslie, 1986; Gorring et al., 1997). First, we describe a suite of key geological, geophysical and geochemical observations for the area. Next, we describe numerical models aimed at addressing how the opening of a slab window and migration of partial melts might affect such observables. Finally, we compare the results of the numerical models with the observations from South America.

2. Geological Setting

2.1. Tectonic Setting and Geological Record

The Chile Ridge (Nazca-Antarctica spreading ridge) subducts below South America at an oblique angle to the trench, resulting in a northward migration of the CTJ since 15 Ma (S. C. Cande & Leslie, 1986; S. C. Cande et al., 1987; Herron et al., 1981). The separation of the Nazca slab progressively led to the continuous opening of the interpreted slab window beneath the continent (Figure 1a). Large differences in the convergence rate between the Nazca and Antarctic plates relative to South America control the geometry of the slab window opening (Tebbens & Cande, 1997). However, the precise slab window geometry is still under debate and several models have been proposed (Bourgois & Michaud, 2002; Breitsprecher & Thorkelson, 2009; Forsythe et al., 1986; Gorring et al., 1997; Thorkelson, 1996).

In terms of the rock record, the western margin of South America exhibits two remarkable geological features along the segment where the Chile Ridge has subducted: the emplacement of the Taitao Ophiolite complex (Anma et al., 2006; Bourgois et al., 2016; Forsythe et al., 1986; Guivel et al., 1999; Nelson et al., 1993; Veloso et al., 2005) and extensive backarc plateau lavas (Gorring et al., 1997; Kay et al., 1993; Ramos & Kay, 1992; C. R. Stern & Kilian, 1996). The Taitao Ophiolite is composed of a complete sequence expected for an oceanic lithosphere from top to bottom (Forsythe et al., 1986; Nelson et al., 1993) with basaltic compositions ranging from N-MORB (depleted mantle) to enriched compositions (Guivel et al., 1999; Lagabrielle et al., 1994). Coeval with this process, the Taitao granites were emplaced, which are possibly linked to contamination of sediment/basement rocks due to the proximity of the subducting spreading center (Anma et al., 2009).

Abundant Neogene lavas erupted over large areas of the backarc region in Argentina south-east of the CTJ with both MORB and OIB affinities (Figure 1a, Ramos & Kay, 1992; Gorring et al., 1997). In this region, there is a gap of the typical arc-magmatism, which can be found north of the CTJ along the Southern Volcanic Zone (Cembrano & Lara, 2009). Further south, arc-type magmatism is resumed along the Austral Volcanic Zone (~49°S) above the slab edge of the Antarctic plate where adakite rocks are produced by the melting of the young/hot oceanic plates (Kay et al., 1993; C. R. Stern & Kilian, 1996). The distinct magmatism in this region is commonly attributed to slab window formation beneath South America (Gorring et al., 1997; Ramos & Kay, 1992).

2.2. Geophysical Observations

Heat flow measurements in southern South America (Figure 1b) show maximum values exceeding 400 mW/m^2 in the vicinity of the CTJ (Ávila & Dávila, 2018), which is consistent with data acquired at other oceanic spreading ridges (Davies, 2013). Further inland, in the backarc region, the average measured heat flow is 50 mW/m^2 (Ávila & Dávila, 2018), in a range expected for backarc environments. Between these two areas, where most of the measurements are concentrated, only scarce and scattered data were collected by Murdie et al. (1998). These measurements exhibit intermediate values between 80 and 120 mW/m^2 in areas located above the expected slab window. Southeast of the CTJ there is scarce coverage with a few reported values <80 mW/m^2 (Ávila &

10.1029/2023GC010977

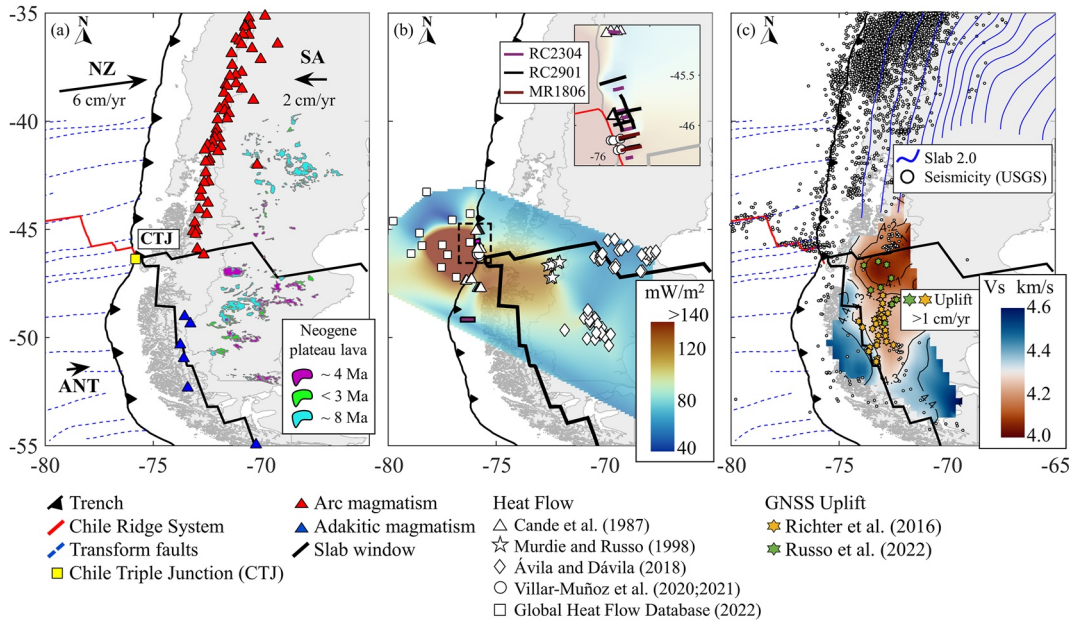

Figure 1. (a) Tectonic setting of the Chile Triple Junction (CTJ), Chile Ridge system and fractures zones according to Maksymowicz et al. (2012), slab window from Breitsprecher and Thorkelson (2009), Neogene plateau lava from Servicio Geológico Minero Argentino and active magmatism from http://volcano.si.edu/. (b) Compiled heat flow map from direct (piston/well; scattered data) and indirect (BSR; lines) measurements, zoom located at the dotted rectangle near the CTJ. (c) Seismic observations along southern South America, Slab 2.0 (Hayes et al., 2018), seismicity (USGS catalog) and shear wave seismic tomography at 100 km depth (Mark et al., 2022), uplift rates on the slab window are also shown in green/yellow stars. NZ, Nazca plate; ANT, Antarctic plate; SA, South American plate. Plate kinematics based on Gao et al. (2023) rotation model using a hotspot reference frame in the GPlates software (http://www.gplates.org/). Colormaps according to Crameri et al. (2020).

Dávila, 2018). To overcome the lack of direct heat flow data in the forearc region, we included, as an additional thermal constraint, the depth of the bottom-simulating reflector (BSR) along the accretionary prism near the CTJ. We compiled the BSR data gathered on two R/V Conrad expeditions (RC2304 and RC2901) and one cruise of the R/V Mirai (MR1806). The studies developed in these expeditions (Bangs & Cande, 1997; K. Brown et al., 1996; S. C. Cande et al., 1987; Villar-Muñoz et al., 2013, 2021) allowed a detailed characterization of the heat flow through the BSR in the vicinity of the CTJ from values that continuously decrease from ∼280 to ∼50 mW/m^2 in the first 50 km from the trench.

Recorded seismicity in this region is sparse (Figure 1c), mostly located in the upper-plate crust (Agurto-Detzel et al., 2014; Suárez et al., 2021). The low rate of seismicity along the plate contact and within oceanic plates is attributed to the low coupling of the Antarctic-South American plate interface and warm conditions of the slabs due to the proximity of the CTJ (Agurto-Detzel et al., 2014; Ávila & Dávila, 2018; Suárez et al., 2021). These warm conditions might extend north up to 38.5°S, enhancing aseismic deformation correlated with the subduction of young oceanic lithosphere <30 Ma (Correa-Otto & Gianni, 2023). As a consequence of low or absent interplate and intraslab seismicity, global subduction zone geometry models do not provide information about the geometry of the slabs south of the CTJ (Figures 1b and 1c, Hayes et al., 2018). Although several models of the slab edges in the slab window area have been proposed (Figure 1b; Bourgois & Michaud, 2002; Breitsprecher & Thorkelson, 2009; Forsythe et al., 1986; Gorring et al., 1997; Thorkelson, 1996), geophysical evidence suggests that the geometry might be larger due to thermal erosion of the slab edges and tearing of the Nazca plate north of the CTJ (Correa-Otto and Gianni, 2023; Navarrete et al., 2020).

Seismic tomography and seismicity provide one of the most robust available constraints on the geometry of the slab window beneath South America, and also help constraining the viscosity structure of the upper mantle, which is further supported by geodetic measurements. P-wave and S-wave velocity models show large (>200 × 200 km) plan-view zones with low velocity anomalies in the mantle (at least from 100 to 200 km depth) coinciding with the interpreted extent of the slab window (Mark et al., 2022; Russo et al., 2010) (Figure 1c). Slab edges can be

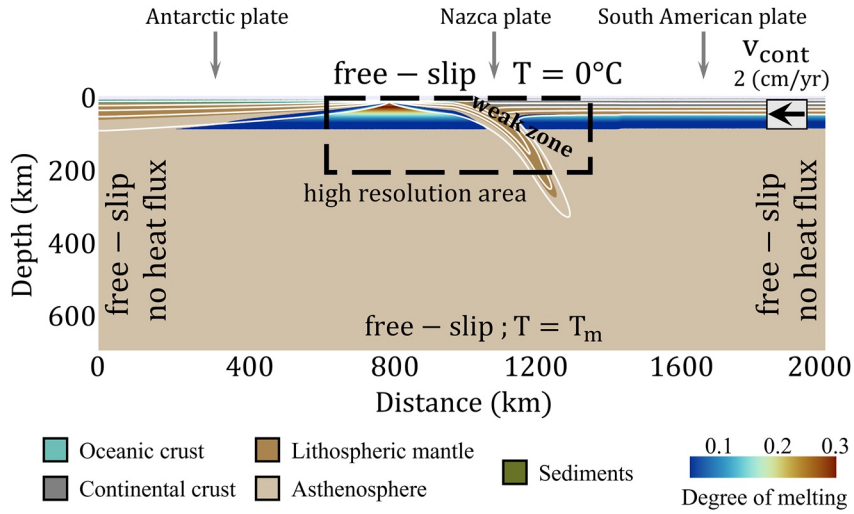

Figure 2. Initial geometry, temperature field and volumetric degree of melting of the numerical model. Background colors represent the domains modeled. Grid resolution in the high-resolution area is 2 km with ~2 million randomly distributed markers. Temperature contours are every 300°C.

inferred south of the CTJ with Mark et al. (2022) model while north of the CTJ, slab tearing of the Nazca plate might enlarge the extent of the slab window (Correa-Otto & Gianni, 2023; Navarrete et al., 2020). Based on seismic velocity variations as a proxy for temperature and viscosity, Mark et al. (2022) estimated mantle viscosities around 10^{19} Pa·s in the slab window low velocity anomaly, while the viscosities increase to $>10^{21}$ Pa·s near the expected Antarctic slab edge. The low viscosity interpreted in the slab window region is consistent with viscosities derived from models of glacial isostatic adjustment of the Patagonian Icefields. Anomalously high surface uplift rates (green and yellow stars in Figure 1c) with a peak >4 cm/yr (Richter et al., 2016; Russo et al., 2022) are consistent with upper mantle viscosities along the slab window area within a range of ~10^{18}–10^{19} Pa·s.

3. Methods

The 2D numerical models were conducted to simulate the mid-ocean ridge subduction within the CTJ tectonic framework. We used a petrological-thermomechanical approach by solving classical geodynamic modeling equations (Turcotte & Schubert, 2014) comprising mass, momentum and energy conservation that are incorporated in the I2ELVIS code (Gerya, 2019; Gerya & Yuen, 2007). In addition, the evolving topography is modeled using the sticky air approach, where this layer simulates a free surface through a low viscosity (10^{18} Pa·s) layer on top of the model (Crameri et al., 2012; Schmeling et al., 2008). Other features in the code include thermodynamic and phase relations for the mantle (Stixrude & Lithgow-Bertelloni, 2011), partial melting (Katz et al., 2003), melt extraction and oceanic lithosphere thickening (e.g., Nikolaeva et al., 2008). Melt fraction tracks the residual partially molten rocks after melt extraction (e.g., Nikolaeva et al., 2008). Finally, the effective rheology for the different domains considers a visco-elasto-plastic approach (e.g., Gerya, 2019; Ranalli, 1995). Further details on the governing equations, the petrological model, partial melting parametrization and rheological parameters are included in Supporting Information S1.

The model setup and initial conditions are summarized in Figure 2. The model domain extends 2,000 × 700 km in the x and y directions, respectively, with a discretization using a variable spacing grid with 401 × 141 nodes. In addition, ~2 million randomly distributed Lagrangian markers are initially prescribed for advecting material properties at every timestep and pressure-temperature condition. The initial temperature field exhibits two major features: the spreading ridge and a subduction zone. The first one is based on oceanic plate cooling models (Stein & Stein, 1992) where the ridge axis is located 200 km from the trench (e.g., Burkett & Billen, 2009; Gerya et al., 2009) where the oceanic lithosphere gets older and thicker away from the spreading center according to the Chile Ridge half-spreading rates (~3 cm/yr; Klitgord et al., 1973; Tebbens et al., 1997). The lithology of the oceanic lithosphere consists of 2 km of basalts, 5 km of gabbros and a variable thickness of mantle lithosphere is set until the 1,000°C isotherm (e.g., Rychert et al., 2020) is reached in the cooling model. The subduction zone

consists of a pre-subducted oceanic plate beneath a continental plate, which represents the geodynamic setting north of the CTJ with the subduction of the Nazca plate beneath the South American plate (Figure 1a). The Nazca plate north of the CTJ is characterized by depths <400 km based on seismic tomography models and seismicity (Correa-Otto & Gianni, 2023; Navarrete et al., 2020). Under this scenario, the initial temperature field is calculated as a steady state solution using the same approach described in Araya Vargas et al. (2021) and Sanhueza et al. (2022) for 2D models using a slab bending geometry for the subducting plate. This subduction zone temperature field generates that the subducting slab 1,000°C isotherm reaches 300 km and subducting velocities of 6–8 cm/yr consistent with the Nazca plate kinematics (Figure 1a). As we do not include a higher viscosity lower mantle (e.g., Burkett & Billen, 2009), deeper initial depths might generate abnormally high subduction velocities. The continental lithosphere is set with a linear geotherm of 30°C/km and is composed of upper crust (20 km), lower crust (15 km) and mantle lithosphere with a base defined by the 1,350°C isotherm. A 10 km thick low-viscosity sticky air layer is used at the top of the model to replicate a free surface as commonly used in previous studies (e.g., Crameri et al., 2012; Schmeling et al., 2008). A 10 km thick slip layer is assigned a viscosity of 10^{20} Pa·s (e.g., Behr et al., 2022; Yáñez & Cembrano, 2004) along the subduction interface to force subduction, which is generated by two driving forces: the slab pull produced by the low temperatures (<1,000°C) and so high densities in the subducting plate and the prescribed velocity of the continental plate (2 cm/yr; South American plate). Velocity and temperature boundary conditions are summarized in Figure 2.

Finally, explored cases and their respective features and aims are detailed in Table 1. These cases consider changes in the rheology of the asthenosphere and partial melt properties (buoyancy and rheology). For the continental lithosphere, we tested different initial thermal gradients which impact the depth of the overriding plate and the magnitude of the prescribed velocity (0 and 6 cm/yr). For the subducting slab, we explored a different initial depth of the pre-subducted slab (200 km). Lastly, we tested a hot asthenosphere case where the upper mantle has a positive temperature anomaly of 100°C that reaches a depth of 200 km.

4. Results

In order to understand geodynamic processes such as slab separation, slab window opening and the subduction of a region of partial melting, we tested several cases similar to those described in Section 3. To simplify the description of the models, we set time $t = 0$ Ma when the mid-ocean ridge is at the trench during the simulation. Therefore, before the ridge collision $t < 0$ and when the mid-ocean ridge starts subducting $t > 0$.

First, we describe the temporal evolution of a reference case (Figure 3) in terms of the melt fraction (residual melt after melt extraction), degree of melting, stream function (flow pattern) and temperature field and the deformation (stress and maximum stress direction; Figure 4) and movement of modeled domains. Then, a parametric study is described in order to compare differences in the spatial extent of the melt fraction and stream function when the mid-ocean ridge is at the trench ($t = 0$ Ma) and 1–2 Ma after the subducted mid-ocean ridge as shown in Figures 5 and 6, respectively.

4.1. Reference Case

The temporal evolution of the reference model can be separated into three distinct stages: (a) prior to the ridge/continent collision (Figure 3, panels a–b), (b) mid-ocean ridge subduction (Figure 3, panels c–h) and (c) post-ridge collision (Figure 3, panels i–l). The first and third stages consist of self-sustaining subduction, while the second one consists of slab separation followed by the slab window opening and subduction of an oceanic lithosphere with zero-absolute motion and age (the Antarctic plate).

The first stage ($t < 0$) is characterized by mid-ocean ridge and subduction zone processes. At the beginning of the simulation (Figure 2), the spatial extent of the zone of partially molten mantle is symmetric with respect to the ridge axis, showing up to 0.35 degree of melting and to 0.04 of melt fraction respectively. This symmetry is consistent with the prescribed initial temperature field (Figure 2), which was calculated using the same half-spreading rate on both sides of the spreading center (3 cm/yr). Beneath the continent, a lower degree of melting is achieved <0.1 (Figure 3, panel B) triggered by the small amount of water content included in the mantle (0.03 wt% or 300 ppm; Green et al., 2010). This zone is located beneath the continental lithosphere in a layer ∼20 km thick. Two types of flow fields are observed. Beneath the mid-ocean ridge, upward velocities are developed along the ridge axis with magnitudes up to 10 cm/yr with a convection cell length of ∼50–80 km. Below

Geochemistry, Geophysics, Geosystems

10.1029/2023GC010977

Table 1
Cases Tested and Detailed Information of Each Model Included in the Parametric Study

Model	Feature	Details	Aim
1	Stronger Asthenosphere	$\eta_{\text{dry-olivine}}$(1 GPa, 1,350°C, 10^{-14}1/s) ≅ 10^{21} Pa·s	Role of mantle rheology
2	Melt without buoyancy	$\rho_{\text{eff}} = \rho_0(P, T)$	Role of rheology and buoyancy in the distribution on partial melts
3	Melt with olivine rheology	$\eta_{\text{melt}} = \eta_{\text{dry-olivine}}(P, T, \dot{\varepsilon})$	
4	Warm continental lithosphere	Continental lithosphere thermal gradient = 40°C/km	Vary the thickness of the continental lithosphere
5	Cold continental lithosphere	Continental lithosphere thermal gradient = 20°C/km	
6	Fixed continent	V_{cont} = 0 cm/yr	Test different kinematics of the overriding plate
7	Fast continent	V_{cont} = 6 cm/yr	
8	Initial slab depth 200 km	Initial slab isotherm 1,000°C at 200 km depth	Lower the Slab pull
9	Hot asthenosphere	dT_{ast} = 100°C until 200 km depth	Study the consequences of a hotter oceanic asthenosphere
Reference case considers:		$\eta_{\text{dry-olivine}}$(1 GPa, 1,350°C, 10^{-14}1/s) ≅ 10^{19} Pa·s $\rho_{\text{eff}} = \rho_0(P, T)\,(1 - M) + M\rho_{\text{melt}} - 0.05\Sigma M_{\text{ext}}$ $\eta_{\text{melt}} = 10^{18}$ Pa·s Continental lithosphere thermal gradient = 30°C/km V_{cont} = 2 cm/yr Initial slab isotherm 1,000°C at 300 km depth $dT_{\text{ast}} = 0$	

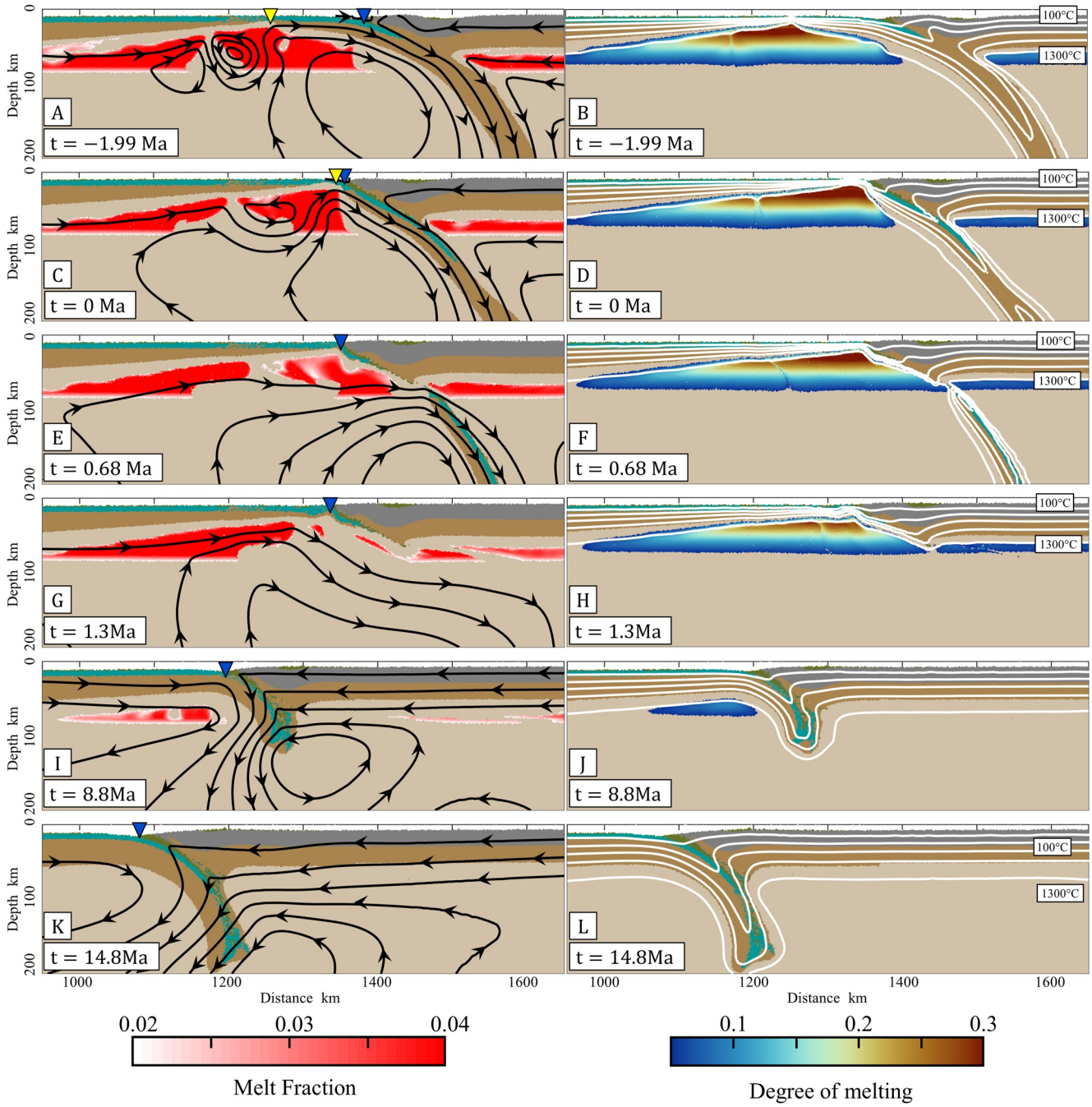

Figure 3. Temporal evolution of the reference case. The left column panels show the stream function (black lines), the melt fraction (red to white zones observed within the asthenosphere), the trench (blue triangle) and the mid-ocean ridge axis (yellow triangle). The right column panels show temperature contours every 300°C (white lines) and the degree of melting (blue to red zones within the asthenosphere) according to the melting parametrization and the petrological model. In all figures, the background colors depict the distribution of the modeled domains according to Figure 2. Time was set at 0 Ma when the mid-ocean ridge is at the trench.

the continent, the subducting slab generates a corner flow velocity field with velocities between 7.5 and 8 cm/yr driven by the negative buoyancy of the subducting slab.

At $t = -1.99$ Ma, the mid-ocean ridge is ~150 km from the trench. In comparison with the initial setup, for this timestep, the zone with a degree of melting >0.2 has diminished its horizontal spatial extent, while its shape is asymmetrical with respect to the ridge axis due to the proximity of the subduction zone (Figure 3, panel b). The stream function also reflects the asymmetry in this stage, where convection cells beneath the mid-ocean ridge

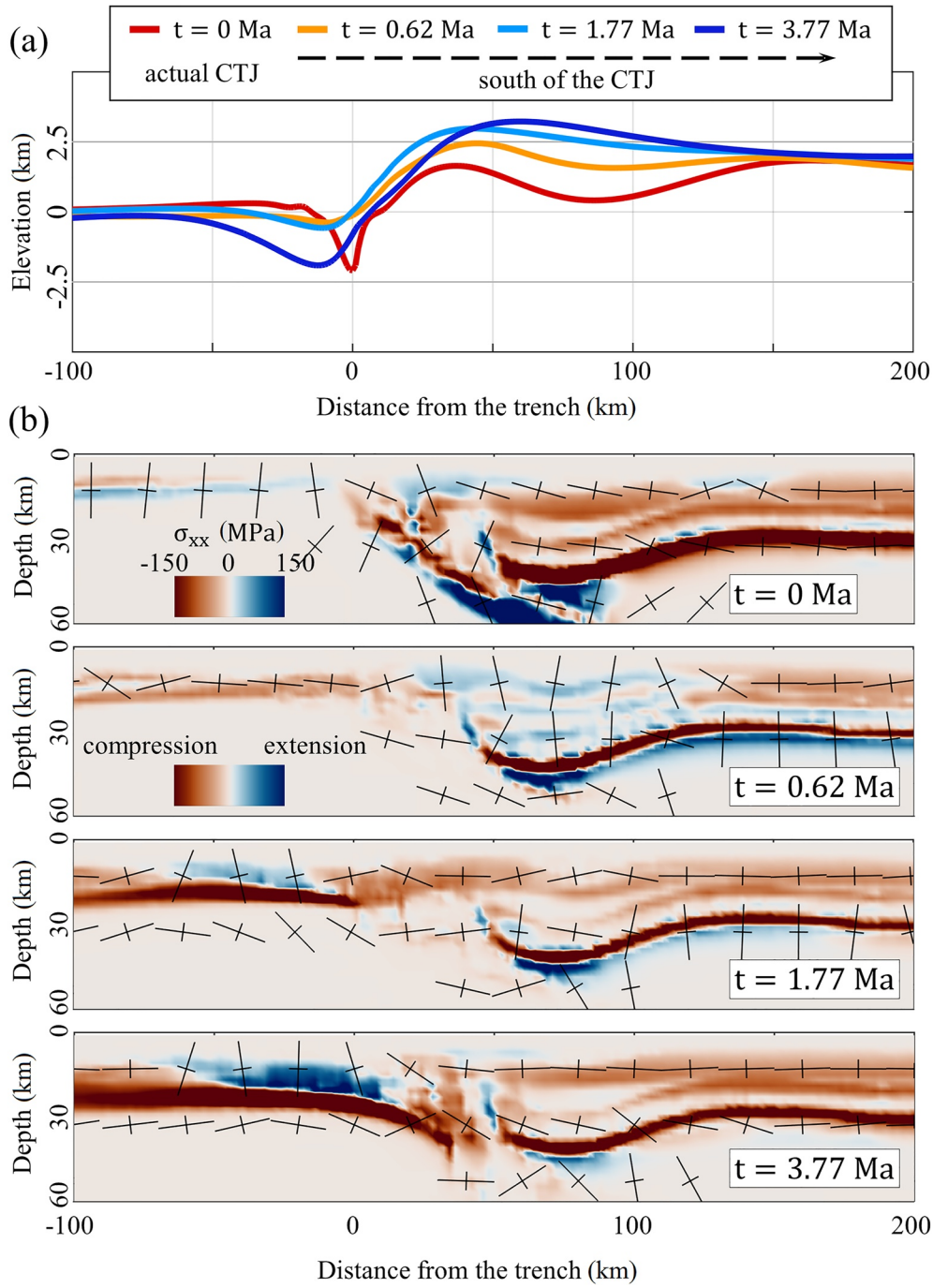

Figure 4. (a) Temporal variations in the topography of the reference model due to the slab separation and subsequent uplift. (b) Temporal evolution of the stress field magnitude (background colors) and maximum stress direction (crosses) during the topographic evolution.

are influenced by the velocity field generated by the subducting slab. In addition, the zone of the mantle with partial melts is dismembered and focused into smaller regions (Figure 3, panel a). The presence of smaller flow cells (black lines in Figure 3a) is driven by the positive buoyancy and lower viscosity of these smaller regions with partial melts.

The second stage comprises the ridge/trench collision within the time range between $0 < t < 1.3$ Ma (Figure 3, panels c–h). In this time interval, the zone with partial melts exhibits a completely asymmetric shape due to the

onset of the mid-ocean ridge subduction at $t = 0$ (Figure 3, panel d). The slab separation is generated right after the mid-ocean ridge collision ($t > 0$; Figure 3, panel c and e) where the slab collapses into the asthenosphere in a short time window due to its negative buoyancy and continuously opens the slab window. The mantle flow is dominated by the motion of the sinking slab (see black lines in Figure 3, panels e and g). The zone with partial melts in the mantle starts to decrease its size and degree of melting because of the subduction initiation of the very young lithosphere and zero absolute motion of the overlying oceanic lithosphere. Some zones with partial melts are observed to the right of the ridge axis, below the continental lithosphere (see melt fraction in Figure 3, panels e and g). The migration of such zones below the continent is forced by the local pressure gradient generated by the sinking slab and the low viscosity assigned to the melt-bearing rocks (10^{18} Pa·s).

The third stage ($t > 1.3$ Ma; Figure 3, panels i–l) occurs after mid-ocean ridge subduction and the onset of the subduction of the zero-absolute motion plate that starts subducting as a young/hot oceanic lithosphere that gets older with time. The main drivers in this setting are the imposed velocity of the continental lithosphere and the negative buoyancy of the oceanic lithosphere, which increases with time as older oceanic plate becomes subducted. Partial melts in the mantle are almost completely exhausted by 8.8 Ma (Figure 3, panel i) and completely exhausted at 14.8 Ma (Figure 3, panel k) because the 1,300°C isotherm becomes deeper than the initial condition and thus, zero degree melting is achieved beneath the continental lithosphere (Figure 3, panels j and l). The streamlines at 8.8 Ma and 14.8 Ma (Figure 3, panel i and k) indicate roll-back of the subducting plate is accompanied by the migration of the trench toward the ocean, driven by the continental plate (1–3 cm/yr).

Overall, the temperature evolution at the subduction zone also depends on the geodynamic stage. Prior to and after the mid-ocean ridge collision, the thermal structure depends on the age and velocity of the subducting plate. At $t = -1.99$ Ma, the 400 and 700°C isotherms within the slab reach a maximum depth of 40 and 170 km respectively (Figure 3, panel a), while at $t = 14.8$ Ma these isotherms reach similar maximum depths of 60 and 140 km respectively (Figure 3, panel l). However, during mid-ocean ridge subduction, large temperature variations are restricted to the forearc, where the asthenosphere is in contact with the subduction interface (Figure 3, panel e). In this region, high temperature gradients are calculated (40–60°C/km) in the first 10 km (Figure 3, panels d, f, and h).

In terms of the temporal evolution of the stress regime in the continental lithosphere, there is a clear correlation between compressional/extensional tectonics with the development of topographic relief (Figure 4). Figure 4a shows the temporal evolution of the topography in the reference model, especially focused on simulation times following the separation of the subducting plate ($t > 0$ Ma). The evolution of the topography shows that following the slab separation (Figure 4a, $t \geq 0$ Ma), the elevation in the forearc increases 1–2 km in comparison with the topography at the mid-ocean ridge collision (Figure 4a, $t = 0$ Ma). The maximum stress direction in the upper crust in our models exhibits significant changes after the slab separation and subsequent mid-ocean ridge subduction. Figure 4b shows cross sections displaying the magnitude of the maximum stress component (background colors) and maximum/minimum stress direction at four snapshots of the reference model. Compressional tectonics (i.e., reddish tones and quasi-horizontal maximum stress direction in Figure 4b) dominate in the forearc upper crust in most of the snapshots. By contrast, after the slab separation ($t = 0.62$ Ma), the model exhibits dominantly extensional stress in the crust at ∼0–100 km from the trench (i.e., blueish tones and sub-vertical maximum stress direction in Figure 7b).

4.2. Parametric Study

Figures 5 and 6 compare the model sections obtained for the reference and alternative cases at $t = 0$ Ma and $t = \sim$1–2 Ma, respectively. In these figures, we show the stream function, temperature field, melt fraction and the surface heat flow for every case. The aim and characteristics of each alternative case are summarized in Table 1.

In comparison with the reference model, case 1 (setup with stronger asthenosphere; Korenaga & Karato, 2008) has a lower subducting slab velocity and a smaller volume of partial melts. Regarding the influence of the physical properties of the melt (Figure 5, cases 2 and 3), both generate a similar spatial extent of partially molten rocks without secondary convection cells (Figure 6, cases 2 and 3). In addition, the stream function is highly dominated by the subducting slab in both cases. The assumed low melt viscosity (10^{18} Pa·s) is 1–3 orders of magnitude lower than mantle viscosity with the dry olivine rheology, while the buoyancy of the melt is in the range of 5–20 kg/m^3. These two factors enhance the development of secondary convection cells beneath the ridge axis as seen in the reference case.

10.1029/2023GC010977

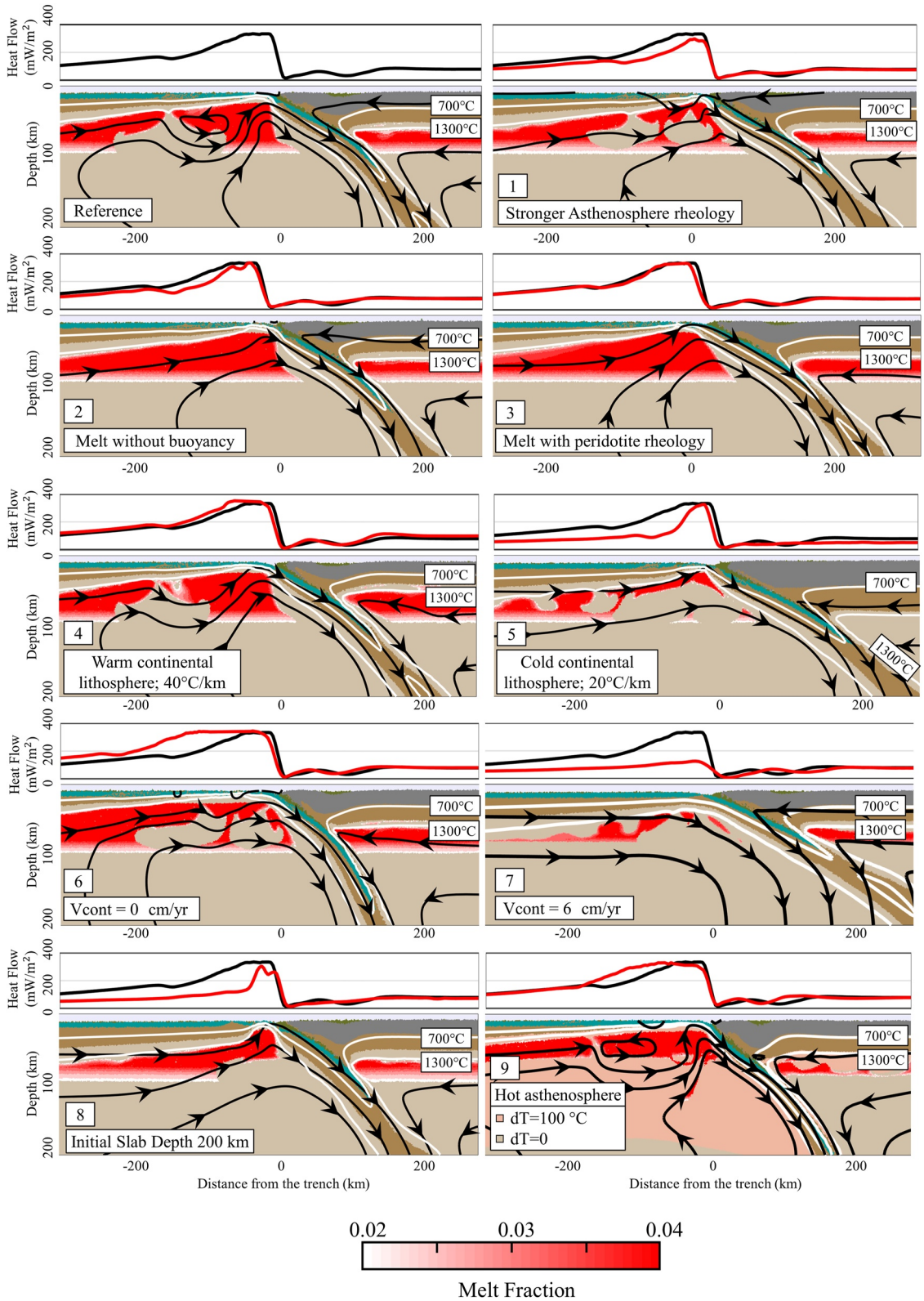

Figure 5. Snapshot at $t = 0$ Ma of all the cases tested. At each case, the upper panel shows the surface heat flow calculated in the first kilometers (the black line = reference case, red line = the corresponding case), while the lower panel shows the section with model results. Two isotherms are shown (700 and 1,300°C), also the stream function and the melt fraction. Lithology colors according to Figure 2.

10.1029/2023GC010977

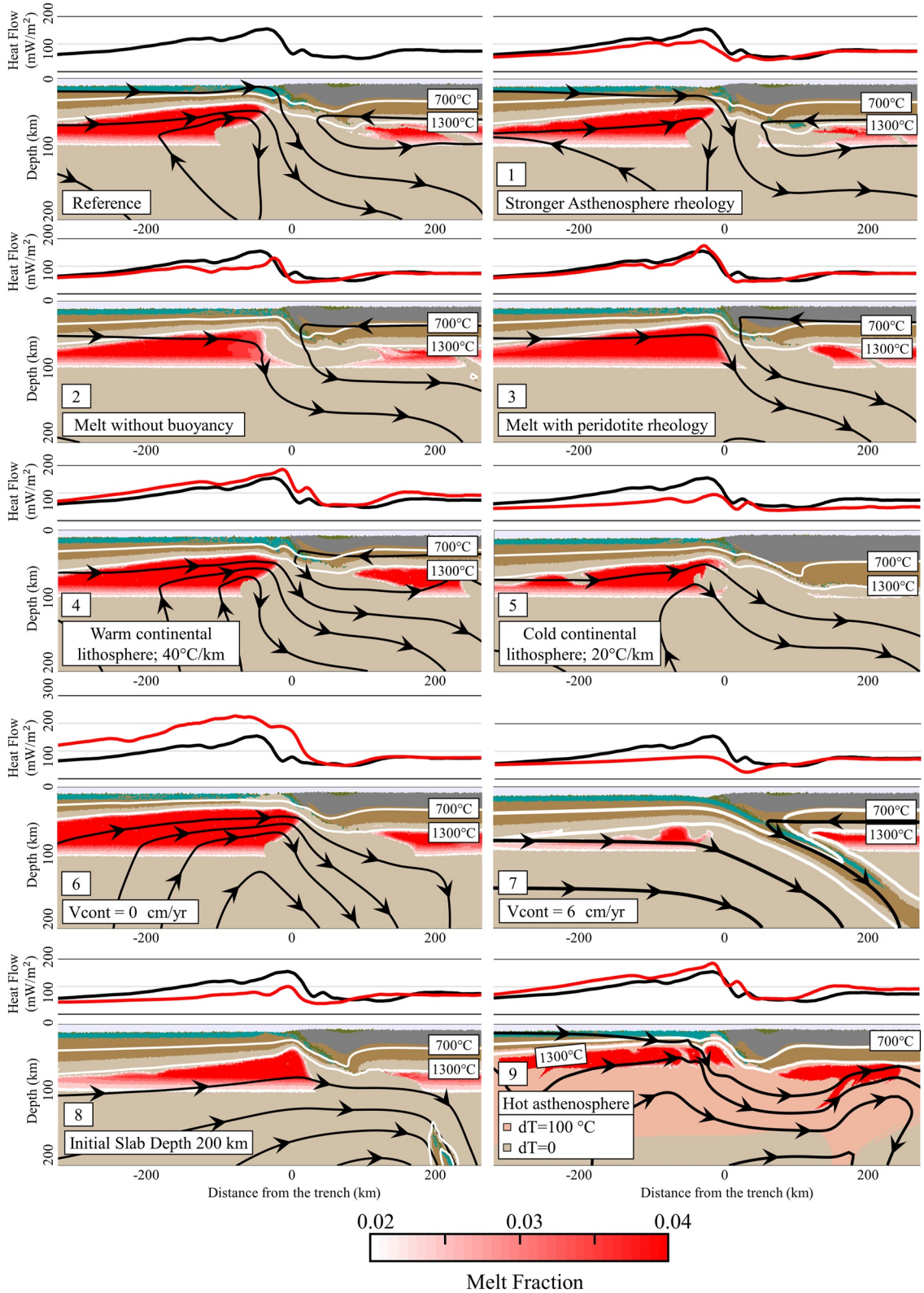

Figure 6. Snapshot at t = ~1–2 Ma of all the cases tested. At each case, the upper panel shows the surface heat flow calculated 6–10 km beneath the top of the oceanic/continental crust (the black line = reference case, red line = the corresponding case), while the lower panel shows the section with model results. Two isotherms are shown (700 and 1,300°C), also the stream function and the melt fraction. Lithology colors according to Figure 2.

The models exploring the thickness of the overriding continental plate reveal differences after the mid-ocean ridge subduction. In the case of a thin continental plate (Figure 5, case 4), the migration of the partially molten rocks from the ridge axis is enhanced due to lower mantle pressures beneath the continental lithosphere and thus, allowing the preservation of a higher volume of partially molten rocks than the reference (Figure 6, case 4). In contrast, a thick continental plate (Figure 5, case 5) represents the opposite case where mantle pressures are higher beneath the continental plate, which prevents the migration and generation of partially molten rocks in this area (Figures 5 and 6, case 5).

Varying the kinematics of the overriding plate directly affects the mid-ocean ridge subduction dynamics. When the overriding plate remains fixed (Figure 5, case 6), the subducting slab develops higher subduction angles. This collapse is faster than the cooling of the mantle, which generates a wide mid-ocean ridge opening as seen in the surface heat flow (Figures 5 and 6, case 6). Conversely, when the continental plate has a velocity of 6 cm/yr (Figure 5, case 7), the opening of the spreading ridge is inhibited, lowering the spatial extent of partially molten rocks both in sub-oceanic and sub-continental mantle. Case 7 is the only scenario where slab separation is not obtained (Figure 6), and consequently no slab window is formed.

Lowering the initial slab depth (Figure 5, case 8) affects both the mid-ocean ridge opening and the subduction zone dynamics. The separated slab in case 8 sinks at a slower velocity than the reference case (compare the position of the separated slab in Figure S1 in Supporting Information S1 for the reference case and Figure 6 case 8). The slab pull is the main force that drives the mid-ocean ridge opening, and thus a lower initial depth is less efficient at opening the mid-ocean ridge.

Finally, the hot asthenosphere case (Figure 5, case 9) shows a zone with partial melting which is larger than in the reference case. The volume of partial melting is increased and secondary convection cells are larger and more vigorous than the reference case due to the higher temperatures imposed in the asthenosphere in this case. Also, at ∼1–2 Ma (Figure 6), after slab window opening, mantle flows from the oceanic to the continental asthenosphere, which allows the generation of a larger volume of partial melts in the subcontinental mantle. The latter process produces a sub-continental upper mantle which is 50–100°C hotter than the reference case.

5. Discussion

5.1. Slab Separation, Slab Window Opening and Mid-Ocean Ridge Dynamics: A Numerical Model Perspective

Mid-ocean ridge subduction facilitates the separation of preceding slabs because the ridge axis represents the weakest part of the system (Gurnis et al., 2004). As a result, the sinking slab decouples from the rest of the oceanic plate along the ridge system, which is the situation observed in all modeled cases, aside from case 7. This case, where the velocity of the overriding plate is too high (i.e., v_{cont} = 6 cm/yr), shows a closure and cooling of the mid-ocean ridge when it approaches the trench and no slab window is generated (see Figures 5 and 6). However, a slab window will always form because the oceanic plates are subducting at different rates and dips, and the presence of transform faults further promotes the widening of slab windows (Dickinson & Snyder, 1979; Thorkelson, 1996). In the CTJ, large differences in subduction rates between the Nazca and Antarctic plates, the presence of fracture zones (Figure 1a) and thermal erosion of the Nazca slab edge (Correa-Otto & Gianni, 2023; Navarrete et al., 2020) are ideal conditions to develop a large-scale slab window under Patagonia (e.g., Breitsprecher & Thorkelson, 2009) under all circumstances.

The interval between the slab separation and when this slab reaches the mantle transition zone (∼670 km) is relatively short (generally <2 Ma; Figure S1 in Supporting Information S1). The sinking slab takes slightly longer time (2–2.5 Ma) to reach the mantle transition zone in case 1 (with stronger asthenosphere) and case 8 (with a smaller initial slab depth of 200 km). As in previous studies (e.g., Burkett & Billen, 2009, 2010), the velocity of sinking slabs is controlled by the viscosity of the asthenosphere and the magnitude of the slab pull force. The immediate consequence of slab separation is the opening of a slab window. Our 2D models represent the fastest slab window opening times as they assume the spreading center is parallel to the trench and a free-slip boundary condition at the bottom of the model (Figure 2). In reality, the oblique subduction of the Chile Ridge implies that the Nazca plate is still subducting north of the CTJ and thus, the slab window opening might last longer

because the Nazca plate prevents a fast sinking of the separated slab, as suggested by our 2D models. In addition, a stronger lower mantle at 670 km depth can support the sinking slab in free subduction models, which reduces the subduction velocity in the order of cm/yr (Burkett & Billen, 2009). In terms of asthenosphere dynamics, the interaction of the subducting slab with the lower mantle is able to explain the Andean orogeny by large-scale mantle circulation (Faccenna et al., 2017). In the case of the separated Nazca plate, longer sinking times might be expected, which can alter the temporal evolution of the flow patterns (Figure 3) and produce more vigorous mantle upwelling.

The flow pattern observed in most of our tested cases suggests the migration of partial melts from the mid-ocean ridge to the base of the continental lithosphere (Figure 6 and Figure S2 in Supporting Information S1), which is clearly shown in the migration of hot asthenosphere particles (dT = 100°C) in case 9 (Figures 5 and 6). Obtained differences in the volume of migrated partially molten rocks are related to the depth of the continental lithosphere (imposed with a thermal gradient until the asthenosphere), the rheology of the melt/asthenosphere and the motion of the overriding plate. As the pressure beneath the continental lithosphere controls the degree of melting (Katz et al., 2003), a warmer/thin continental lithosphere promotes a higher degree of melting due to lower pressures beneath the plate. Water content might also play a role due to the dehydration of the sinking slab (DeLong et al. (1979); Iwamori, 2000) which enhances melting conditions.

Almost all model cases (except case 7) suggest that the asthenosphere beneath the mid-ocean ridge is able to flow beneath the continental lithosphere, which is further assisted by the opposite kinematics of the overriding plate shortly after the slab window opening. In addition, if we take into account the hypothesis of a plume-fed asthenosphere (case 9), the asthenosphere beneath the ocean might achieve higher temperatures than in the continent, where the asthenosphere is consumed (Morgan, 1971; Phipps Morgan et al., 1995). Support for hot suboceanic asthenosphere comes from analysis of seismic observations explained by low amounts of partial melts (0.1%–0.7%) that have been imaged beneath oceans up to 200–250 km (Debayle et al., 2020). Simple models of the flow of the hot asthenosphere can explain the variations in the depth of plate spreading centers (Buck et al., 2009). For this setup (case 9), horizontal transport of a higher temperature asthenosphere during the slab window opening is more efficient than upwelling in producing higher temperatures and so larger volumes of partial melting beneath the continental lithosphere.

Models without melt buoyancy and with a peridotite rheology (cases 2 and 3, respectively) do not show the typical mid-ocean ridge corner flow with an upward flow below the ridge axis (e.g., Buck & Su, 1989; Spiegelman & McKenzie, 1987). Contrarily, the other cases exhibit smaller convection cells beneath the mid-ocean ridge axis (Figures 3 and 5). Consequently, the buoyancy and low viscosity assigned to the partially molten rocks capture the first-order process seen in more complex simulations of two-phase flow (e.g., Katz, 2008, 2010, 2022) and therefore represent more accurately magma dynamics.

5.2. Temperature Constraints: Heat Flow, Metamorphism, and Magmatic Record

We compared the heat flow calculated from the modeled temperature distribution with heat flow data obtained from measurements, proxies and independent theoretical models. In the area where the Chile Ridge has not collided with the trench ($t < 0$ in the models), the calculated heat flow at surface was compared with two theoretical cooling models of the oceanic lithosphere: the Composite Young Hydrothermal model (CYH1) of Stein et al. (1995) and the cooling models for young oceanic lithosphere of Qiuming (2016). In these theoretical models, we used the half-spreading rate of the Chile Ridge (3 cm/yr; Klitgord et al., 1973; Tebbens et al., 1997). The comparison for $t = -1.95$ Ma and the mentioned ridge cooling models is shown in Figure 7a. The good match left of the ridge axis is expected because the initial temperature field on the oceanic lithosphere in our models is calculated using the Stein and Stein (1992) approach, which is the basis of the two theoretical cooling models plotted in Figure 7a. This match shows that the modeled temporal evolution of the heat flow and temperature field of the mid-ocean ridge before the collision is consistent with analytical models.

10.1029/2023GC010977

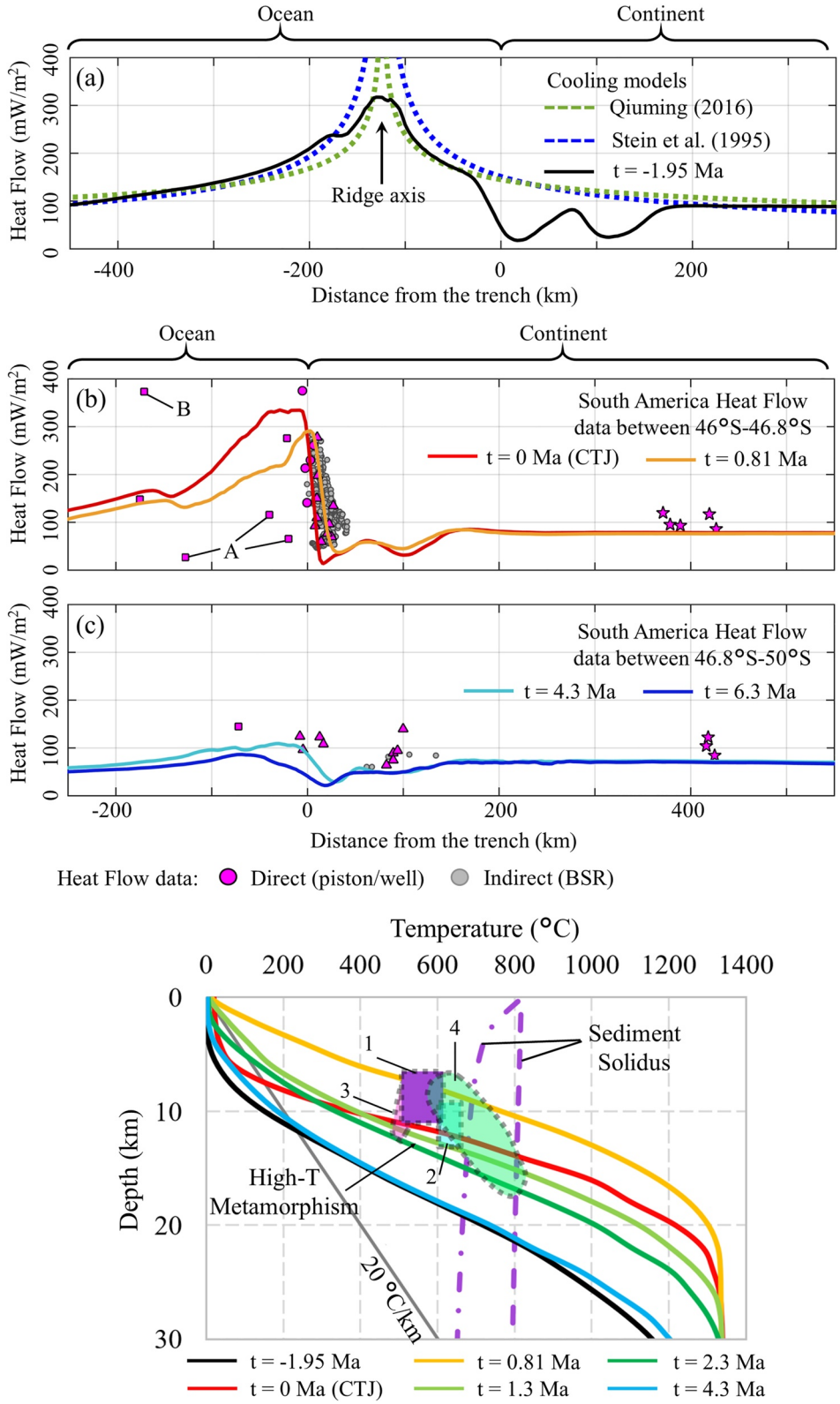

Figure 7. Comparison between the calculated heat flow (reference case) and (a) theoretical models of mid-ocean ridge cooling for young oceanic lithospheres, (b) heat flow data measured north of 46.8°S, and (c) heat flow data measured south of 46.8°S. The heat flow data legend is according to Figure 1b. (d) Temperature profiles (reference case) at the trench in a time window $-1.95 < t < 4.3$ Ma. Purple dotted lines represent two sediment solidus curves. Transparent polygons are metamorphic conditions along the forearc in Japan (1), the northern Cordillera of Alaska (2) and British Columbia (3) and the north China Craton (4) (see text for details).

The CTJ has migrated northwards by ~700 km since it started subducting at 15 Ma (S. C. Cande & Leslie, 1986; Gorring et al., 1997). Thus, the temporal evolution of our 2D models during and after the mid-ocean ridge subduction can be compared with the thermal structure at latitudes south of the CTJ where the Chile Ridge system already subducted in a nearly parallel direction with respect to the trench. This correlation between times after the subducted mid-ocean ridge in the models ($t > 0$) and latitudes south of the CTJ is based on the reconstructions of the CTJ in the last 15 Ma (Figure S3 in Supporting Information S1). The present mid-ocean ridge segment subducting the margin is between 46°S and 46.8°S where its south end started subducting 0.8 Ma. South of 46.8°S, the last subducted ridge segment occurred 3.3 Ma (S. C. Cande & Leslie, 1986; Maksymowicz et al., 2012). Therefore, the heat flow calculated from our models in the time frame of $0 < t < 0.8$ Ma (i.e., the interval where the mid-ocean ridge is at the trench and starts subducting) was compared with heat flow data observed at 46°S–46.8°S (Figure 7b). Following the same rationale, we compared the calculated and observed heat flow south of the 46.8°S with associated times in our models $t > 3.3$ Ma (i.e., when the Antarctic plate is already subducting) according to the last subducted ridge segment south of this latitude (Figure 7c).

Figure 7b shows a good match between the heat flow calculated from our models (lines) and the observed heat flow data (symbols; direct and indirect). Most of the observed heat flow data are concentrated in the offshore part, where the heat flow exhibits a sharp decrease from values of ~400 mW/m^2 (near the trench) down to ~50 mW/m^2 (ca. 50 km landwards from the trench). This sharp decrease has been attributed to the progressive thickening of the continental lithosphere in the landward direction (S. C. Cande et al., 1987), which is a much colder block (<100 mW/m^2) than the mid-ocean ridge (300 mW/m^2). In the Pacific, some heat flow observations are poorly fitted by the model between −200 and 0 km from the trench (Figure 7b). This apparent mismatch is because those heat flow data are located either far from the ridge segment currently at the trench at 46°S–46.8°S (e.g., points labeled A in Figure 7b) or close to segments of the mid-ocean ridge which are located offshore north of 46°S (e.g., points labeled B in Figure 7b). In the continent, near the General Carrera Lake (approximately 400 km from the trench in Figure 7b), there is a slight difference between the calculated and observed heat flow (~80 and ~100 mW/m^2, respectively). This difference can be related to the circulation of hydrothermal fluids in the upper crust, which enhances the local heat flow. The presence of hot springs in the vicinity of the General Carrera Lake (Negri et al., 2018) and possible heat sources in the upper crust support the hypothesis of hydrothermal circulation in this part of the continent (Lagarrigue et al., 2021). It is worth to remind that hydrothermal circulation was not included in our models.

Figure 7c shows the comparison between the heat flow calculated from the model and heat flow observations located at latitudes where the last ridge segment subducted prior to 3.3 Ma. At this time window ($t > 3.3$ Ma) the heat flow signature from the mid-ocean ridge is greatly diminished. In fact, the calculated heat flow is <100 mW/m^2, values which are typical from forearc regions in cold subduction zones (e.g., Currie & Hyndman, 2006). In Figure 7c, modeled heat flow values consistently underestimate the observed data. Comparatively higher values in observed heat flow can be also attributed to the advection of heat by the circulation of hydrothermal fluids, hypothesis which is consistent with the presence of hydrothermal activity suggested by previous studies (S. C. Cande et al., 1987; Villar-Muñoz et al., 2021).

We also evaluated the reliability of the modeled temperature distribution by analyzing thermal proxies derived from records of metamorphism and magmatism in the forearc. Figure 7d shows the temporal evolution of the temperature profile at the trench before (−1.95 Ma), during (0 and 0.83 Ma) and after (1.3, 2.3, and 4.3 Ma) the mid-ocean ridge subduction. In addition, Figure 7d shows metamorphic conditions recorded in areas of other margins where a subducted mid-ocean ridge has been inferred: the Izanagi triple junction in Japan (polygon 1; M. Brown, 1998; Hiroi et al., 1998), and segments of the northern Cordillera of Alaska (polygon 2; Sisson & Pavlis, 1993; Sisson et al., 1989) and British Columbia (polygon 3; Groome et al., 2003) and the north China Craton (polygon 4; Zhao, 2014). Finally, Figure 7d also shows the sediment solidus characteristic based on wet metasediments (Auzanneau et al., 2006; Nichols et al., 1994).

Before and after the mid-ocean ridge subduction, the ongoing subduction of oceanic slabs in the model reproduces the subduction of the Nazca and Antarctic plates with the corresponding convergence rates of 5–7 and 2 cm/yr respectively. At these stages, the temperature profiles are controlled by the subducting slab which advects cold isotherms, generating a low thermal gradient in the forearc (R. J. Stern, 2002). This is correctly reproduced by our models at $t = -1.95$ Ma and $t = 4.3$ Ma, where a thermal gradient of <15°C/km is obtained in the upper crust (Figure 7d). As a consequence of the proximity of the mid-ocean ridge to the trench, Figure 7d at 0 and

0.81 Ma shows thermal gradients >40°C/km during the mid-ocean ridge subduction, values which are significantly higher than the stages before (−1.95 Ma) and after (4.3 Ma) subduction. The increase in the thermal gradient in the forearc generates temperatures of 500–700°C at depths of 15–20 km (0.5 GPa; 5 kbar). These conditions are consistent with the high temperature metamorphic conditions recorded in modern forearcs of the northern Cordillera and ancient forearcs in Japan and north China (polygons in Figure 7d). In addition, the emplacement of the Taitao Ophiolite complex ca. 5 Ma is coeval with the emplacement of the Taitao granites (Anma & Orihashi, 2013; Anma et al., 2009; Veloso et al., 2005). Anma et al. (2009) suggested that the source of these magmas might be related to sediment or upper crust melting during the past subducted ridge segments, which potentially elevated the temperatures in the forearc. Our results are highly consistent with this hypothesis because the sediment solidus is achieved at shallow depths (∼15 km; Figure 7d). The melting of sediments might also affect the sediment thickness at the trench, generating erosional phases near the CTJ as suggested by Bangs and Cande (1997). South of the CTJ, sediments accumulate at the trench (S. C. Cande et al., 1987; Olsen et al., 2020) which is reproduced with an increase in the sediment thickness at the trench in Figure 3 (dark-green domain in panels i and k).

Summarizing, the temporal evolution of the thermal structure of our models is consistent with the surface heat flow in space and time. Our model results suggest that the subduction of an active ridge is able to generate high temperature metamorphism and even magmatism in the forearc region. Such magmatism can be derived from the melting of subducted sediments and/or of the upper plate crust. Although the heat flow calculated from our model shows an overall good fit of observations, there are some segments where the quality of the fit is poorer, likely due to second-order heat transport processes which are not accounted by our modeling approach (e.g., hydrothermal circulation, ophiolite emplacement and metamorphic endothermic/exothermic reactions) or the role of 3D effects in the flow field that might affect the temperature field in the upper crust in a much larger area as suggested by Christiansen et al. (2022) extending north of the CTJ from the arc to backarc regions.

5.3. Slab Window Upper Mantle: Reconciling Geophysical Observations and Geochemistry

Seismic and geodetic evidence suggest that the upper mantle exhibits distinctive temperature and rheological conditions in the area interpreted for the slab window (according to the kinematic model of Breitsprecher & Thorkelson, 2009). Seismic studies have imaged within the slab window region anomalously low *P*-wave and *S*-wave seismic velocity at depths ≥100 km (Mark et al., 2022; Russo et al., 2010). Geodetic studies have recorded high uplift rates in the continent (Richter et al., 2016; Russo et al., 2022), which have been attributed to the deglaciation of the Patagonian Ice Fields and the presence of low viscosities (10^{18}–10^{19} Pa·s) within the upper mantle (Russo et al., 2022). Russo et al. (2022) propose an along-margin rheological segmentation of the slab window, where the northern and younger segment (near the CTJ) is characterized by lower viscosities (∼10^{18} Pa·s), while the southern and older segment is slightly stronger (∼10^{19} Pa·s).

The distinctive physical conditions of the upper mantle within the slab window have been attributed to the upwelling of the higher temperature asthenosphere during the slab window opening (Gorring et al., 1997), and to the erosion of the lithospheric mantle (Mark et al., 2022). In our models, the development of upward velocities in the asthenosphere is a short-lasting process <2 Ma associated with the slab separation (Figure 3, black lines in panels C and E). After the mid-ocean ridge subduction (Figure 3, panels g–l), we do not observe notable temperature changes within the asthenosphere due to upwelling, suggesting that a short-duration upwelling is not capable of bringing deeper parts of the mantle to shallower depths (<100 km). In contrast, a strong flow pattern from the oceanic to the continental mantle is observed (Figure 3, panels e and g). Such horizontal movements of the low-viscosity asthenosphere appear to be more efficient at changing the temperatures under the continent.

Figure 8a shows the shear wave velocity (V_s) distribution in a cross-section at 48°S, taken from the seismic model of Mark et al. (2022). Figure 8b shows sections at the same equivalent position of Figure 8a, but V_s is calculated using information from the snapshot at t = 1–2 Ma of three model cases: the reference case and two cases, which predict the larger volumes of partially molten rocks migrated from the mid-ocean ridge (cases 4 and 9 in Figure 6). The calculated V_s sections were computed according to the stable mineral assemblage at a given pressure-temperature condition based on the anhydrous mantle minerals database (Stixrude & Lithgow-Bertelloni, 2011) and a 5% reduction in the velocity where partially molten rocks are present in our models (e.g., Lyakhovsky et al., 2021). Figure 8c shows the effective viscosity of the asthenosphere taken from the same model section, cases, and simulation time shown in Figure 8b. Both the observed and calculated distribution of V_s show that the center and eastern segment of the section are dominated

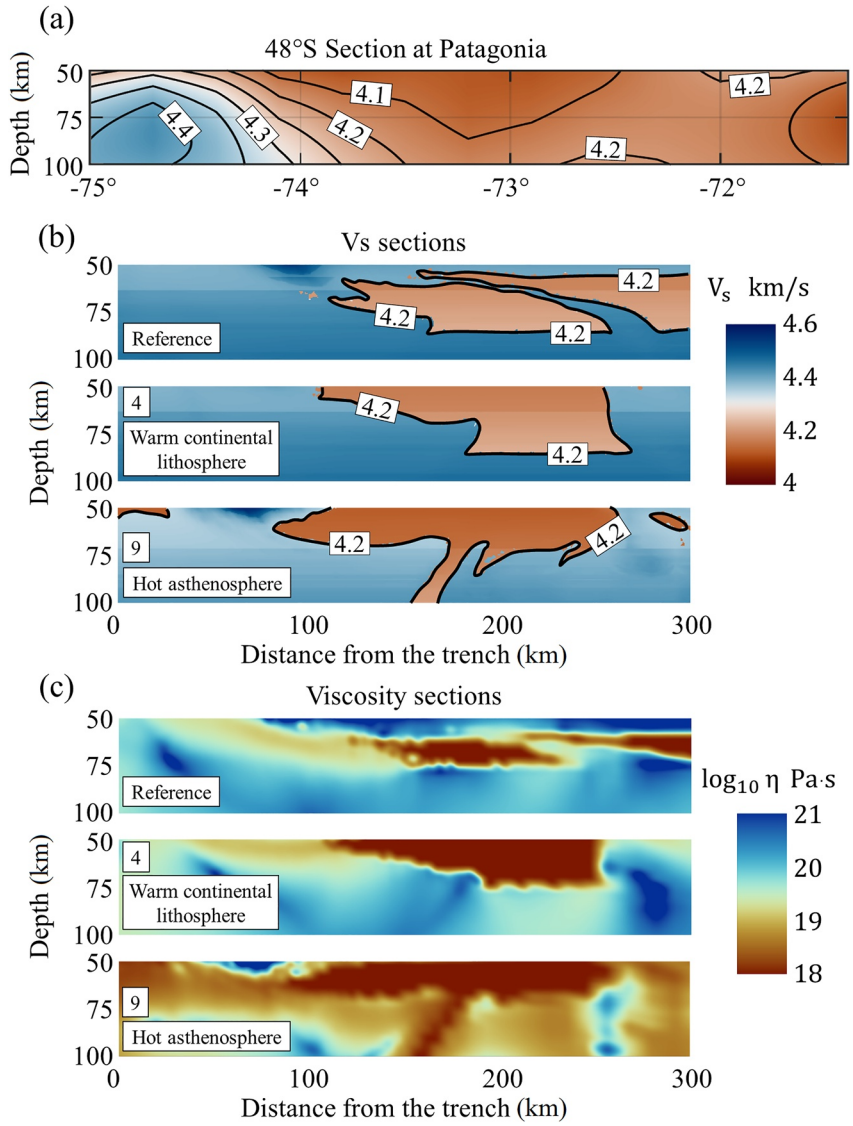

Figure 8. (a) Shear wave seismic velocity (V_s) cross section at 48°S taken from the seismic model of Mark et al. (2022). (b) V_s distribution calculated using the petrological composition of three model cases at simulation time t = 1–2 Ma (see text for details). (c) Effective viscosity sections taken from the same models and simulation time shown in (b).

by comparatively lower values (V_s < 4.2 km/s, reddish zones in Figures 8a and 8b). As the areas of low calculated V_s are located in regions where the modeled cases suggest the presence of partial melts (see Figure 6, reference case and cases 4 and 9), we suggest that observed low V_s values imaged by Mark et al. (2022) can be related to the presence of partial melts. These low values of V_s, therefore, suggest that partially molten rocks might be present beneath the South American lithosphere. This process is compatible with the possibility of eroding the lithospheric mantle as suggested by Mark et al. (2022).

Partially molten rocks that migrated from the Chile Ridge, are more likely to be preserved over several million years under a thin continental lithosphere setup (case 4) and/or if the asthenosphere under the Pacific has a positive temperature anomaly (case 9). The presence of partially molten rocks also controls the viscosity of the upper mantle (Figure 8c) that might provide suitable conditions to develop efficient visco-elastic rebounds that can explain the anomalously high uplift rates on the surface of the slab window. Viscosities are even further lowered for case 9, where the oceanic asthenosphere down to 300 km is assumed to be hotter than the deeper mantle (case 9), generating effective viscosities in the range of 10^{18}–10^{19} Pa·s, consistent with the findings of Russo et al. (2022).

Finally, the migration of partially molten rocks from the subducted mid-ocean ridge to the subcontinental mantle can be further supported by the geochemical signature of the Chile Ridge system, the Taitao Ophiolite complex and the backarc plateau lavas emplaced over the slab window during the Neogene (Figure 1a; Ramos & Kay, 1992; Gorring et al., 1997). Overall, the isotopic compositions of the Chile Ridge are similar along different spreading segments, where depleted MORB compositions are observed (Bach et al., 1996). The depletion of the mantle is included in the models by the successive melt extraction episodes (e.g., Nikolaeva et al., 2008) that continuously deplete the underlying asthenosphere at the mid-ocean ridge before the ridge collision. After the mid-ocean ridge subduction (Figure 3, panel e and g), the migration of a depleted mantle source (partially molten) from the mid-ocean ridge implies that the magmas beneath the South American plate might preserve a similar geochemical signature observed in other ridge segments of the Chile Ridge and in the backarc magmatism. This is consistent with the similar chemical composition of magmas of the Taitao Ridge, the Taitao Peninsula and the Chile Ridge, which suggest a common source (Guivel et al., 1999). Moreover, the noble gas composition of mantle xenoliths (spinel and/or garnet bearing) of alkaline basalts in the backarc show MORB-like signatures and in some cases, show also $^{3}He/^{4}He$ ratios which are similar to the North Chile Ridge MORB samples (Jalowitzki et al., 2016). In addition, the signature of Sr-Nd isotope compositions of backarc basaltic lavas erupted above the slab window region also suggest a depleted mantle source (D'Orazio et al., 2001). However, the depleted mantle source that migrates from the mid-ocean ridge is also controlled by the contamination of the trailing end of the Nazca slab, which releases fluids and incompatible elements, producing an OIB-like geochemical signature on the backarc lavas (Gorring et al., 1997; D'Orazio et al., 2001; Gorring & Kay, 2001).

5.4. Uplift, Tectonics, and Generation of Forearc Slivers

Aside from better understood consequences of the subduction of the Chile Ridge beneath South America (i.e., the lack of arc magmatism and slab seismicity), the anomalously high summit elevations and relief south of the CTJ have received much attention in the recent years. No consensus has emerged and different models have been proposed based on analog experiments (Guillaume et al., 2010), dynamic topography modeling (Braun et al., 2013; Guillaume et al., 2013; Hollyday et al., 2023), and thermochronology (Thomson et al., 2010) combined with structural data (Georgieva et al., 2016). Thomson et al. (2010) propose that the high topographic relief is mainly generated by latitudinal climate changes, which control the efficiency on glacial erosion north and south of the CTJ. Meanwhile, dynamic topography models suggest that the replacement of the cold subducting slab with asthenosphere is the main mechanism to generate large topographic uplift (Guillaume et al., 2013), which extends further inland in the backarc (Guillaume et al., 2009; Hollyday et al., 2023; Pedoja et al., 2011). Finally, Georgieva et al. (2016) suggest an important role for strike-slip tectonics near the CTJ with the generation of forearc slivers controlling the high summit at the Northern Patagonian Icefield.

Our models are consistent with the increased elevation being caused by the slab break-off as seen by previous numerical and analog models (e.g., Buiter et al., 2002; Duretz et al., 2011, 2012; Guillaume et al., 2010, 2013). In our case, the increase in elevation is caused by the separation and descent of the subducting slab, where the inflow of asthenosphere material fills the gap left by the now sunken slab. In addition, there is a clear switch in the tectonic regime, where compressional tectonics are present before and after the mid-ocean ridge subduction (Figure 4b and Figure S4b in Supporting Information S1), consistent with subduction zone environments (e.g., R. J. Stern, 2002) related to the Nazca-South America and Antarctica-South America margins. However, during mid-ocean ridge subduction, extensional tectonics are observed that coincides with the increase in elevation (Figure 4b and Figure S4b in Supporting Information S1). These results are consistent with the stress regime north of the CTJ, which is mainly compressional and transpressional along the Liquiñe-Ofqui Fault Zone (Cembrano et al., 1996; Cembrano & Lara, 2009). This change in the stress regime suggests a significant stress rotation triggered by the topographic uplift. The rotation of the principal stress in the upper crust is also observed in numerical models of the slab break-off process that do not involve mid-ocean ridge subduction (Duretz et al., 2011, 2012). In the vicinity of the CTJ, Forsythe and Nelson (1985) identified normal faulting in Golfo de Penas basin, where multiple ridge segments collided at 0.3, 3, and 6 Ma. These normal faults are also linked to a forearc sliver (Chiloé block) that generates the partitioning of the deformation caused by the oblique subduction of the Nazca plate (Cembrano et al., 2002; Nelson et al., 1994). The Chiloé block moves northwards, generating extension in the southern end located at Golfo de Penas area, and contraction to the north in the Arauco region (Melnick et al., 2009). Recently, Georgieva et al. (2016), proposed that the generation of these forearc slivers are triggered by the successive mid-ocean ridge collisions. This idea is supported by our model results, where

Table 2
Comparison of Every Case With the Constraints Available in the Chile Triple Junction

		Constraints for:		
Model	Feature	Temperature	Upper Mantle physical properties	Deformation/stress in the continent
Reference	–	✓	o	✓
1	Stronger Asthenosphere	o	✗	o
2	Melt without buoyancy	✗	✗	✗
3	Melt with olivine rheology	✓	✗	o
4	Warm continental lithosphere	✓	✓	✓
5	Cold continental lithosphere	o	✗	o
6	$V_{cont} = 0$ cm/yr	✗	✗	✗
7	$V_{cont} = 6$ cm/yr	✗	✗	✗
8	Initial slab depth 200 km	o	o	o
9	Hot asthenosphere	✓	✓	✓
Indicators:	✓ Consistent with data		o Correlated with data	✗ No correlation

the mechanism to generate a forearc sliver is the topographic response and the rotation of the maximum stress direction after the slab separation. This is consistent with extensional faulting in Golfo de Penas area (south of the CTJ; Forsythe & Nelson, 1985) and the northward migration of the CTJ (S. C. Cande & Leslie, 1986), which might have triggered the generation of the Chiloé block in the past. The extensional stress regime developed in the forearc due to mid-ocean ridge subduction might explain the generation of forearc slivers in southern South America and south of the CTJ (e.g., Georgieva et al., 2016).

5.5. Preferred Model for the Chile Triple Junction

Table 2 summarizes the comparison between all the modeled cases and the observations used as constrain. The observations were categorized in terms of how they constraint the spatiotemporal distribution of temperature (heat flow measurements and metamorphic record), upper mantle physical properties (seismic anomaly and viscosity structure) and deformation/stress in the continent (topography uplift and fault kinematics). For every category, we defined three indicators based on consistency (matching tendency and magnitude), correlation (only tendency) and no correlation with data.

In terms of temperature, cases 1, 2, 5, and 8 have similar heat flow curves at $t = 0$ Ma (Figure 5) but the heat flow curve rapidly decays at later times (Figure 6). Conversely, the reference case and cases 3, 4, 9 are consistent with the heat flow data in term of magnitude and time (Figures 5 and 7b). Cases 6 and 7 are two end-members either with anomalous high heat flow (case 6) or low heat flow (case 7) (Figure 5). Also, case 7 shows no slab window opening, which contradicts the basic principles of slab window formation (e.g., Dickinson & Snyder, 1979; Thorkelson, 1996). Regarding constraints for the physical properties of the upper mantle, cases 4 and 9 better explain the low seismic anomalies and low viscosity (Figure 8). This better correlation is due to larger volumes of partial melts beneath the subcontinental mantle obtained in these cases, which is a consequence of a more vigorous mantle flow from the spreading center beneath the subcontinental mantle (Figure 6). Cases 2, 8 and the reference also obtain migration of partial melts into

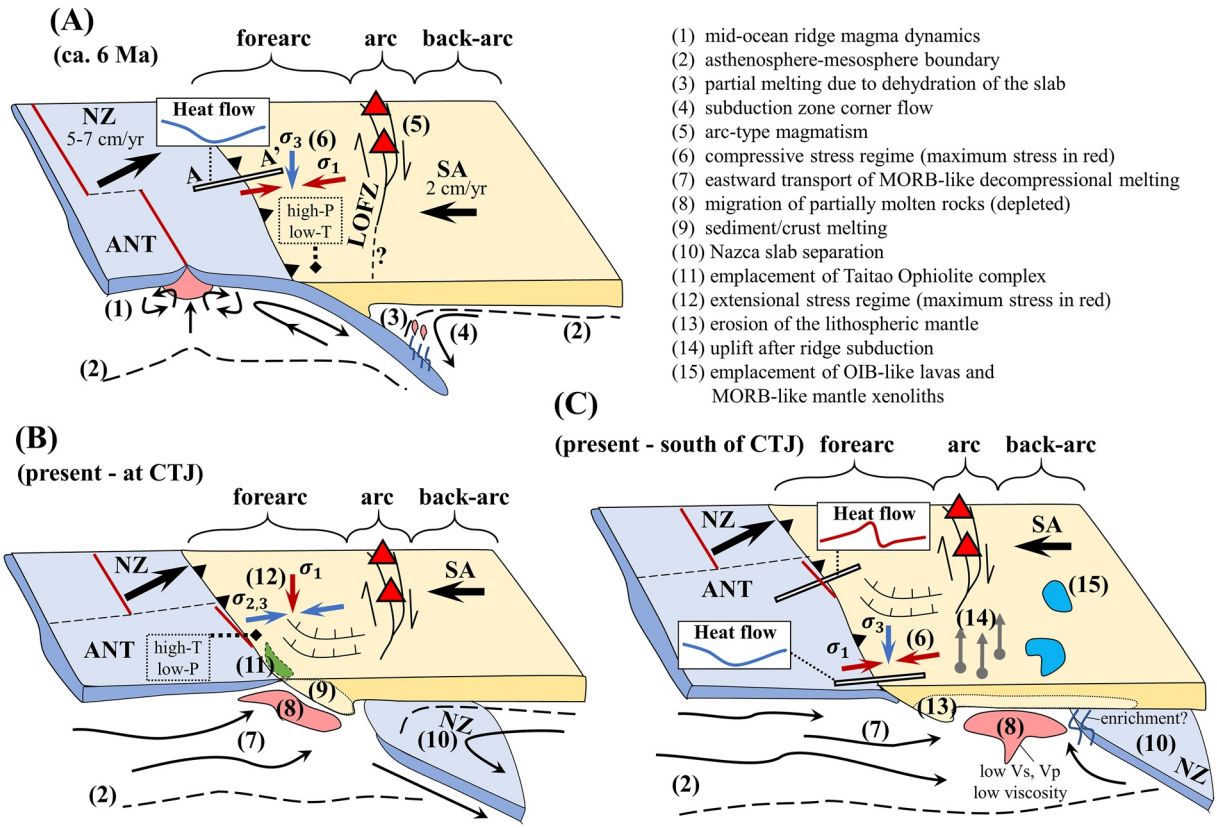

Figure 9. Cartoon showing the temporal evolution of the Chile Triple Junction (CTJ) and the consequences due to the ridge subduction and slab window opening processes beneath South America at the latitude of the Taitao Peninsula (45°S–50°S). (a) Tectonic setting and processes of the Nazca-South America subduction zone before the subduction of a segment of the Chile Ridge. (b) and (c) show the processes and consequences of the ridge subduction process at the latitude of the present position of the CTJ (during ridge subduction) and south of the CTJ (after ridge subduction) on the Antarctica-South America subduction zone, respectively. NZ, Nazca plate; ANT, Antarctica plate; SA, South American plate; LOFZ, Liquiñe-Ofqui Fault Zone. Tectonic setup and assumptions based on a warm/thin continental lithosphere and the presence of a hot asthenosphere.

the subcontinental mantle, but resulting in smaller volumes (Figure 6). Topography uplift (considered as a proxy for deformation) is observed in all cases aside of case 7 because continental uplift is a consequence of slab separation and slab window opening. After slab separation, extensional tectonics are developed in all cases (except case 7) where the reference case (Figure 4b) and cases 4 and 9 (Figure S4 in Supporting Information S1) show the clearest rotation of the maximum stress direction. Case 6 is discarded because it evolves to a passive margin after the slab separation due to the lack of driving forces on both plates. Summarizing, the models with a warm/thin continental lithosphere (case 4) and the hot asthenosphere (case 9) reproduce geodynamics evolution scenarios that are more consistent with the geological, geophysical and geochemical proxies available for the CTJ.

6. Conclusions

The petrological-thermomechanical numerical models obtained in this study correctly account for first order geological and geophysical observations in the CTJ region. In addition, our results provide quantitative explanations to understand the interplay between the subduction of the Chile Ridge, the development of the slab window, and the distinctive tectonic, magmatic and metamorphic processes inferred in this segment of the South American margin. This knowledge might be applicable to other modern/ancient slab windows and mid-ocean ridge subduction environments. The preferred model that explains most of the geological, geophysical and geochemical proxies are a warm/thin continental lithosphere (case 4) and a hot asthenosphere (case 9). The proposed temporal evolution of the CTJ and the consequences are summarized in Figure 9, which has the following implications:

The heat flow in the vicinity of the CTJ, where a mid-ocean ridge segment is currently subducting, is characterized by a sharp decrease from 400 mW/m^2 down to 40 mW/m^2 in the forearc. South of the CTJ, the low heat flow is consistent with the ongoing subduction and roll-back of the Antarctic plate. The ridge subduction process is a viable mechanism to generate high-temperature/low-pressure metamorphism and magmatism associated with the melting of sediments or continental crust within the forearc during the subduction of the ridge. The presence of partially molten rocks that migrated from the ridge to beneath the overriding plate might be able to explain the low seismic velocity anomalies beneath South America. Moreover, these melt-bearing rocks decrease the upper mantle viscosity, which provides suitable conditions to develop high uplift rates recorded on the surface. After slab separation, an uplift of the forearc is predicted by the models, process which explains the higher topography south of the CTJ. Coeval with the forearc uplift, the development of extensional tectonics provides a mechanism to explain the decoupling and generation of forearc slivers.

Data Availability Statement

The I2ELVIS code is available at Gerya and Yuen (2007) and Gerya (2019). Geological maps from Argentina are available at https://sigam.segemar.gov.ar/geonetwork39. Heatflow data were collected from public repositories for R/V Conrad expeditions: RC2901 (S. Cande, 2012) and RC2304 (S. Cande, 2010), International Heat Flow Commission: https://ihfc-iugg.org/products/global-heat-flow-database/data and the corresponding references in the main text. The shear wave seismic tomography from Mark et al. (2022) is available at Mark et al. (2021). Plate rotations and kinematics based on Gao et al. (2023) model. Colormaps of Crameri et al. (2020) are available at Crameri (2023).

Acknowledgments
We are grateful to Steve Cande for encouraging discussions and reviews on the BSR data and the reconstructions of the CTJ. Sofia Lagarrigue is acknowledged for giving insights on the heat flow measurements in South America. Andrei Maksymowicz and Eduardo Contreras-Reyes are acknowledged for sharing their detailed mapping of oceanic structures for the reconstruction. We thank Hannah Mark for discussing the resolution and sensitivity of the shear wave seismic tomography. Amol Sawant is also acknowledged for suggesting geochemical proxies for the discussions. Jorge Sanhueza was supported by a PhD Scholarship from ANID 21210747 and the FONDECYT project 1201354, both granted by the Chilean government. We thank the editorial handling of Claudio Faccenna and meaningful reviews of Derek Thorkelson, Guido Gianni and an anonymous reviewer who helped to improve the clarity and quality of the manuscript.

References

Agurto-Detzel, H., Rietbrock, A., Bataille, K., Miller, M., Iwamori, H., & Priestley, K. (2014). Seismicity distribution in the vicinity of the Chile triple Junction, Aysén region, southern Chile. *Journal of South American Earth Sciences*, *51*, 1–11. https://doi.org/10.1016/j.jsames.2013.12.011

Anma, R., Armstrong, R., Danhara, T., Orihashi, Y., & Iwano, H. (2006). Zircon sensitive high mass-resolution ion microprobe U-PB and fission-track ages for gabbros and sheeted Dykes of the Taitao ophiolite, southern Chile, and their tectonic implications. *Island Arc*, *15*(1), 130–142. https://doi.org/10.1111/j.1440-1738.2006.00513.x

Anma, R., Armstrong, R., Orihashi, Y., Ike, S., Shin, K., Kon, Y., et al. (2009). Are the Taitao granites formed due to subduction of the Chile ridge? *Lithos*, *113*(1–2), 246–258. https://doi.org/10.1016/j.lithos.2009.05.018

Anma, R., & Orihashi, Y. (2013). Shallow-depth melt eduction due to ridge subduction: LA-ICPMS U-PB igneous and detrital zircon ages from the Chile triple Junction and the Taitao peninsula, Chilean Patagonia. *Geochemical Journal*, *47*(2), 149–165. https://doi.org/10.2343/geochemj.2.0243

Araya Vargas, J., Sanhueza, J., & Yáñez, G. (2021). The role of temperature in the along-margin distribution of volcanism and seismicity in subduction zones: Insights from 3-D Thermomechanical modeling of the central Andean margin. *Tectonics*, *40*(11), e2021TC006879. https://doi.org/10.1029/2021tc006879

Auzanneau, E., Vielzeuf, D., & Schmidt, M. W. (2006). Experimental evidence of decompression melting during exhumation of subducted continental crust. *Contributions to Mineralogy and Petrology*, *152*(2), 125–148. https://doi.org/10.1007/s00410-006-0104-5

Ávila, P., & Dávila, F. M. (2018). Heat flow and lithospheric thickness analysis in the Patagonian asthenospheric Windows, southern South America. *Tectonophysics*, *747–748*, 99–107. https://doi.org/10.1016/j.tecto.2018.10.006

Bach, W., Erzinger, J., Dosso, L., Bollinger, C., Bougault, H., Etoubleau, J., & Sauerwein, J. (1996). Unusually large NbTa depletions in north Chile ridge basalts at 36°50′ to 38°56′S: Major element, trace element, and isotopic data. *Earth and Planetary Science Letters*, *142*(1–2), 223–240. https://doi.org/10.1016/0012-821x(96)00095-7

Bangs, N. L., & Cande, S. C. (1997). Episodic development of a convergent margin inferred from structures and processes along the southern Chile margin. *Tectonics*, *16*(3), 489–503. https://doi.org/10.1029/97tc00494

Barker, F., Farmer, G. L., Ayuso, R. A., Plafker, G., & Lull, J. S. (1992). The 50 Ma granodiorite of the eastern Gulf of Alaska: Melting in an accretionary prism in the forearc. *Journal of Geophysical Research*, *97*(B5), 6757. https://doi.org/10.1029/92jb00257

Behr, W. M., Holt, A. F., Becker, T. W., & Faccenna, C. (2022). The effects of plate interface rheology on subduction kinematics and dynamics. *Geophysical Journal International*, *230*(2), 796–812. https://doi.org/10.1093/gji/ggac075

Bourgois, J., Lagabrielle, Y., Martin, H., Dyment, J., Frutos, J., & Cisternas, M. E. (2016). A review on Forearc ophiolite Obduction, adakite-like generation, and slab window development at the Chile triple Junction area: Uniformitarian framework for spreading-ridge subduction. *Pageoph Topical Volumes*, 3217–3246. https://doi.org/10.1007/978-3-319-51529-8_2

Bourgois, J., & Michaud, F. (2002). Comparison between the Chile and Mexico triple Junction areas substantiates slab window development beneath northwestern Mexico during the past 12–10 Myr. *Earth and Planetary Science Letters*, *201*(1), 35–44. https://doi.org/10.1016/s0012-821x(02)00653-2

Braun, J., Robert, X., & Simon-Labric, T. (2013). Eroding dynamic topography. *Geophysical Research Letters*, *40*(8), 1494–1499. https://doi.org/10.1002/grl.50310

Breitsprecher, K., & Thorkelson, D. J. (2009). Neogene kinematic history of Nazca–Antarctic–Phoenix slab windows beneath Patagonia and the Antarctic Peninsula. *Tectonophysics*, *464*(1–4), 10–20. https://doi.org/10.1016/j.tecto.2008.02.013

Brown, K., Bangs, N., Froelich, P., & Kvenvolden, K. (1996). The nature, distribution, and origin of gas hydrate in the Chile triple Junction region. *Earth and Planetary Science Letters*, *139*(3–4), 471–483. https://doi.org/10.1016/0012-821x(95)00243-6

Brown, M. (1998). Ridge-trench interactions and high- T -low-P metamorphism, with particular reference to the Cretaceous evolution of the Japanese islands. *Geological Society, London, Special Publications*, *138*(1), 137–169. https://doi.org/10.1144/gsl.sp.1996.138.01.09

Buck, W. R., Small, C., & Ryan, W. B. (2009). Constraints on asthenospheric flow from the depths of oceanic spreading centers: The east Pacific rise and the Australian-Antarctic discordance. *Geochemistry, Geophysics, Geosystems*, *10*(9), Q09007. https://doi.org/10.1029/2009gc002373

Buck, W. R., & Su, W. (1989). Focused mantle upwelling below mid-ocean ridges due to feedback between viscosity and melting. *Geophysical Research Letters*, *16*(7), 641–644. https://doi.org/10.1029/gl016i007p00641

Buiter, S. J., Govers, R., & Wortel, M. (2002). Two-dimensional simulations of surface deformation caused by slab detachment. *Tectonophysics*, *354*(3–4), 195–210. https://doi.org/10.1016/s0040-1951(02)00336-0

Burkett, E. R., & Billen, M. I. (2009). Dynamics and implications of slab detachment due to ridge-trench collision. *Journal of Geophysical Research*, *114*(B12), B12402. https://doi.org/10.1029/2009jb006402

Burkett, E. R., & Billen, M. I. (2010). Three-dimensionality of slab detachment due to ridge-trench collision: Laterally simultaneous boudinage versus tear propagation. *Geochemistry, Geophysics, Geosystems*, *11*, 11. https://doi.org/10.1029/2010gc003286

Cande, S. (2010). Ship-based trackline geophysical data (MGD77) acquired during the Robert D. Conrad expedition RC2304 (1982) [Dataset]. Interdisciplinary Earth Data Alliance (IEDA). https://doi.org/10.1594/IEDA/315192

Cande, S. (2012). Multi-Channel seismic shot data from the southern Chile Trench acquired during the R/V Robert D. Conrad expedition RC2901 (1988) [Dataset]. Interdisciplinary Earth Data Alliance (IEDA). https://doi.org/10.1594/IEDA/318861

Cande, S. C., & Leslie, R. B. (1986). Late Cenozoic tectonics of the southern Chile trench. *Journal of Geophysical Research*, *91*(B1), 471. https://doi.org/10.1029/jb091ib01p00471

Cande, S. C., Leslie, R. B., Parra, J. C., & Hobart, M. (1987). Interaction between the Chile ridge and Chile trench: Geophysical and geothermal evidence. *Journal of Geophysical Research*, *92*(B1), 495. https://doi.org/10.1029/jb092ib01p00495

Cembrano, J., Hervé, F., & Lavenu, A. (1996). The Liquiñe Ofqui fault zone: A long-lived intra-arc fault system in southern Chile. *Tectonophysics*, *259*(1–3), 55–66. https://doi.org/10.1016/0040-1951(95)00066-6

Cembrano, J., & Lara, L. (2009). The link between volcanism and tectonics in the southern volcanic zone of the Chilean Andes: A review. *Tectonophysics*, *471*(1–2), 96–113. https://doi.org/10.1016/j.tecto.2009.02.038

Cembrano, J., Lavenu, A., Reynolds, P., Arancibia, G., López, G., & Sanhueza, A. (2002). Late Cenozoic transpressional ductile deformation north of the Nazca–south America–Antarctica triple Junction. *Tectonophysics*, *354*(3–4), 289–314. https://doi.org/10.1016/s0040-1951(02)00388-8

Chadwick, J., Perfit, M., McInnes, B., Kamenov, G., Plank, T., Jonasson, I., & Chadwick, C. (2009). Arc lavas on both sides of a trench: Slab window effects at the Solomon Islands triple junction, SW Pacific. *Earth and Planetary Science Letters*, *279*(3–4), 293–302. https://doi.org/10.1016/j.epsl.2009.01.001

Christiansen, R. O., Gianni, G. M., Ballivián Justiniano, C. A., García, H. P., & Wohnlich, S. (2022). The role of geotectonic setting on the heat flow distribution of southern South America. *Geophysical Journal International*, *230*(3), 1911–1927. https://doi.org/10.1093/gji/ggac161

Correa-Otto, S., & Gianni, G. M. (2023). Lower and upper plate controls on crustal seismicity in the southern central and Patagonian Andes. *Tectonics*, *42*(1), e2022TC007335. https://doi.org/10.1029/2022tc007335

Crameri, F. (2023). Scientific colour maps (8.0.0) [Maps]. *Zenodo*. https://doi.org/10.5281/zenodo.8035877

Crameri, F., Schmeling, H., Golabek, G. J., Duretz, T., Orendt, R., Buiter, S. J., et al. (2012). A comparison of numerical surface topography calculations in geodynamic modelling: An evaluation of the 'sticky air' method. *Geophysical Journal International*, *189*(1), 38–54. https://doi.org/10.1111/j.1365-246x.2012.05388.x

Crameri, F., Shephard, G. E., & Heron, P. J. (2020). The misuse of colour in science communication. *Nature Communications*, *11*(1), 5444. https://doi.org/10.1038/s41467-020-19160-7

Currie, C. A., & Hyndman, R. D. (2006). The thermal structure of subduction zone back arcs. *Journal of Geophysical Research*, *111*(B8), B08404. https://doi.org/10.1029/2005jb004024

Davies, J. H. (2013). Global map of solid earth surface heat flow. *Geochemistry, Geophysics, Geosystems*, *14*(10), 4608–4622. https://doi.org/10.1002/ggge.20271

Debayle, E., Bodin, T., Durand, S., & Ricard, Y. (2020). Seismic evidence for partial melt below tectonic plates. *Nature*, *586*(7830), 555–559. https://doi.org/10.1038/s41586-020-2809-4

DeLong, S. E., & Fox, P. J. (1977). Geological consequences of ridge subduction. *Island Arcs, Deep Sea Trenches and Back-Arc Basins*, 221–228. https://doi.org/10.1029/me001p0221

DeLong, S. E., Schwarz, W. M., & Anderson, R. N. (1979). Thermal effects of ridge subduction. *Earth and Planetary Science Letters*, *44*(2), 239–246. https://doi.org/10.1016/0012-821x(79)90172-9

Dickinson, W. R., & Snyder, W. S. (1979). Geometry of subducted slabs related to San Andreas transform. *The Journal of Geology*, *87*(6), 609–627. https://doi.org/10.1086/628456

D'Orazio, M., Agostini, S., Innocenti, F., Haller, M., Manetti, P., & Mazzarini, F. (2001). Slab window-related magmatism from southernmost South America: The late Miocene mafic volcanics from the Estancia Glencross area (~52°S, Argentina–Chile). *Lithos*, *57*(2–3), 67–89. https://doi.org/10.1016/s0024-4937(01)00040-8

Duretz, T., Gerya, T. V., & May, D. A. (2011). Numerical modelling of spontaneous slab breakoff and subsequent topographic response. *Tectonophysics*, *502*(1–2), 244–256. https://doi.org/10.1016/j.tecto.2010.05.024

Duretz, T., Schmalholz, S. M., & Gerya, T. V. (2012). Dynamics of slab detachment. *Geochemistry, Geophysics, Geosystems*, *13*(3), 2453. https://doi.org/10.1029/2011gc004024

Faccenna, C., Oncken, O., Holt, A. F., & Becker, T. W. (2017). Initiation of the Andean orogeny by lower mantle subduction. *Earth and Planetary Science Letters*, *463*, 189–201. https://doi.org/10.1016/j.epsl.2017.01.041

Forsythe, R., & Nelson, E. (1985). Geological manifestations of ridge collision: Evidence from the Golfo de Penas-Taitao Basin, southern Chile. *Tectonics*, *4*(5), 477–495. https://doi.org/10.1029/tc004i005p00477

Forsythe, R. D., Nelson, E. P., Carr, M. J., Kaeding, M. E., Herve, M., Mpodozis, C., et al. (1986). Pliocene near-trench magmatism in southern Chile: A possible manifestation of ridge collision. *Geology*, *14*(1), 23. https://doi.org/10.1130/0091-7613(1986)14<23:pnmisc>2.0.co;2

Furlong, K. P., & Schwartz, S. Y. (2004). Influence of the Mendocino Triple Junction on the Tectonics of coastal California. *Annual Review of Earth and Planetary Sciences*, *32*(1), 403–433. https://doi.org/10.1146/annurev.earth.32.101802.120252

Gao, L., Zhao, Y., Yang, Z., Pei, J., Zhang, S.-H., Liu, X., et al. (2023). Plate rotation of the northern Antarctic Peninsula since the Late Cretaceous: Implications for the tectonic evolution of the scotia sea region. *Journal of Geophysical Research: Solid Earth*, *128*(2), e2022JB026110. https://doi.org/10.1029/2022JB026110

Georgieva, V., Melnick, D., Schildgen, T. F., Ehlers, T. A., Lagabrielle, Y., Enkelmann, E., & Strecker, M. R. (2016). Tectonic control on rock uplift, exhumation, and topography above an oceanic ridge collision: Southern patagonian Andes (47°S), Chile. *Tectonics*, *35*(6), 1317–1341. https://doi.org/10.1002/2016tc004120

Gerya, T. V. (2019). *Introduction to numerical geodynamic modelling*. Cambridge University Press.
Gerya, T. V., Fossati, D., Cantieni, C., & Seward, D. (2009). Dynamic effects of aseismic ridge subduction: Numerical modelling. *European Journal of Mineralogy*, *21*(3), 649–661. https://doi.org/10.1127/0935-1221/2009/0021-1931
Gerya, T. V., & Yuen, D. A. (2007). Robust characteristics method for modelling multiphase Visco-elasto-plastic thermo-mechanical problems. *Physics of the Earth and Planetary Interiors*, *163*(1–4), 83–105. https://doi.org/10.1016/j.pepi.2007.04.015
Gorring, M. L., & Kay, S. M. (2001). Mantle processes and sources of Neogene slab window magmas from southern Patagonia, Argentina. *Journal of Petrology*, *42*(6), 1067–1094. https://doi.org/10.1093/petrology/42.6.1067
Gorring, M. L., Kay, S. M., Zeitler, P. K., Ramos, V. A., Rubiolo, D., Fernandez, M. I., & Panza, J. L. (1997). Neogene Patagonian plateau lavas: Continental magmas associated with ridge collision at the Chile triple Junction. *Tectonics*, *16*(1), 1–17. https://doi.org/10.1029/96tc03368
Green, D. H., Hibberson, W. O., Kovács, I., & Rosenthal, A. (2010). Water and its influence on the lithosphere–asthenosphere boundary. *Nature*, *467*(7314), 448–451. https://doi.org/10.1038/nature09369
Groome, W. G., & Thorkelson, D. J. (2009). The three-dimensional thermo-mechanical signature of ridge subduction and slab window migration. *Tectonophysics*, *464*(1–4), 70–83. https://doi.org/10.1016/j.tecto.2008.07.003
Groome, W. G., Thorkelson, D. J., Friedman, R. M., Mortensen, J. K., Massey, N. W., Marshall, D. D., & Layer, P. W. (2003). Magmatic and tectonic history of the Leech river complex, Vancouver Island, British Columbia: Evidence for ridge-trench intersection and accretion of the crescent terrane. Geology of a transpressional orogen developed during ridge-trench interaction along the North Pacific margin. https://doi.org/10.1130/0-8137-2371-x.327
Guillaume, B., Gautheron, C., Simon-Labric, T., Martinod, J., Roddaz, M., & Douville, E. (2013). Dynamic topography control on Patagonian relief evolution as inferred from low temperature thermochronology. *Earth and Planetary Science Letters*, *364*, 157–167. https://doi.org/10.1016/j.epsl.2012.12.036
Guillaume, B., Martinod, J., Husson, L., Roddaz, M., & Riquelme, R. (2009). Neogene uplift of central eastern Patagonia: Dynamic response to active spreading ridge subduction? *Tectonics*, *28*(2), TC2009. https://doi.org/10.1029/2008tc002324
Guillaume, B., Moroni, M., Funiciello, F., Martinod, J., & Faccenna, C. (2010). Mantle flow and dynamic topography associated with slab window opening: Insights from laboratory models. *Tectonophysics*, *496*(1–4), 83–98. https://doi.org/10.1016/j.tecto.2010.10.014
Guivel, C., Lagabrielle, Y., Bourgois, J., Maury, R., Fourcade, S., Martin, H., & Arnaud, N. (1999). New geochemical constraints for the origin of ridge-subduction-related plutonic and volcanic suites from the Chile triple Junction (Taitao peninsula and site 862, LEG ODP141 on the Taitao ridge). *Tectonophysics*, *311*(1–4), 83–111. https://doi.org/10.1016/s0040-1951(99)00160-2
Gurnis, M., Hall, C., & Lavier, L. (2004). Evolving force balance during incipient subduction. *Geochemistry, Geophysics, Geosystems*, *5*(7), Q07001. https://doi.org/10.1029/2003gc000681
Hayes, G. P., Moore, G. L., Portner, D. E., Hearne, M., Flamme, H., Furtney, M., & Smoczyk, G. M. (2018). Slab2, a comprehensive subduction zone geometry model. *Science*, *362*(6410), 58–61. https://doi.org/10.1126/science.aat4723
Herron, E. M., Cande, S. C., & Hall, B. R. (1981). *An active spreading center collides with a subduction zone: A geophysical survey of the Chile margin triple junction* (pp. 683–702). Geological Society of America Memoirs. https://doi.org/10.1130/mem154-p683
Hiroi, Y., Kishi, S., Nohara, T., Sato, K., & Goto, J. (1998). Cretaceous high-temperature rapid loading and unloading in the Abukuma metamorphic terrane, Japan. *Journal of Metamorphic Geology*, *16*(1), 67–81. https://doi.org/10.1111/j.1525-1314.1998.00065.x
Hole, M. J., & Larter, R. D. (1993). Trench-proximal volcanism following ridge crest-trench collision along the Antarctic Peninsula. *Tectonics*, *12*(4), 897–910. https://doi.org/10.1029/93tc00669
Hollyday, A., Austermann, J., Lloyd, A., Hoggard, M., Richards, F., & Rovere, A. (2023). A revised estimate of early Pliocene global mean sea level using geodynamic models of the Patagonian slab window. *Geochemistry, Geophysics, Geosystems*, *24*(2), e2022GC010648. https://doi.org/10.1029/2022GC010648
Iannelli, S. B., Fernández Paz, L., Litvak, V. D., Gianni, G., Fennell, L. M., González, J., et al. (2020). Southward-directed subduction of the Farallon–Aluk spreading ridge and its impact on subduction mechanics and Andean arc magmatism: Insights from geochemical and seismic tomographic data. *Frontiers in Earth Science*, *8*, 121. https://doi.org/10.3389/feart.2020.00121
Iwamori, H. (2000). Thermal effects of ridge subduction and its implications for the origin of granitic batholith and paired metamorphic belts. *Earth and Planetary Science Letters*, *181*(1–2), 131–144. https://doi.org/10.1016/s0012-821x(00)00182-5
Jalowitzki, T., Sumino, H., Conceição, R. V., Orihashi, Y., Nagao, K., Bertotto, G. W., et al. (2016). Noble gas composition of subcontinental lithospheric mantle: An extensively degassed reservoir beneath southern Patagonia. *Earth and Planetary Science Letters*, *450*, 263–273. https://doi.org/10.1016/j.epsl.2016.06.034
Johnston, S. T., & Thorkelson, D. J. (1997). Cocos-Nazca slab window beneath central America. *Earth and Planetary Science Letters*, *146*(3–4), 465–474. https://doi.org/10.1016/s0012-821x(96)00242-7
Katz, R. F. (2008). Magma dynamics with the enthalpy method: Benchmark solutions and magmatic focusing at mid-ocean ridges. *Journal of Petrology*, *49*(12), 2099–2121. https://doi.org/10.1093/petrology/egn058
Katz, R. F. (2010). Porosity-driven convection and asymmetry beneath mid-ocean ridges. *Geochemistry, Geophysics, Geosystems*, *11*(11), Q0AC07. https://doi.org/10.1029/2010gc003282
Katz, R. F. (2022). *The dynamics of partially molten rock*. Princeton University Press.
Katz, R. F., Spiegelman, M., & Langmuir, C. H. (2003). A new parameterization of hydrous mantle melting. *Geochemistry, Geophysics, Geosystems*, *4*(9), 173. https://doi.org/10.1029/2002gc000433
Kay, S. M., Ramos, V. A., & Marquez, M. (1993). Evidence in Cerro Pampa volcanic rocks for slab-melting prior to ridge-trench collision in southern South America. *The Journal of Geology*, *101*(6), 703–714. https://doi.org/10.1086/648269
Kimura, G., Kitamura, Y., Yamaguchi, A., Kameda, J., Hashimoto, Y., & Hamahashi, M. (2019). Origin of the early Cenozoic belt boundary thrust and Izanagi–Pacific ridge subduction in the western Pacific margin. *Island Arc*, *28*(5), e12320. https://doi.org/10.1111/iar.12320
Klitgord, K., Mudie, J., Larson, P., & Grow, J. (1973). Fast sea-floor spreading on the Chile ridge. *Earth and Planetary Science Letters*, *20*(1), 93–99. https://doi.org/10.1016/0012-821x(73)90144-1
Korenaga, J., & Karato, S. (2008). A new analysis of experimental data on olivine rheology. *Journal of Geophysical Research*, *113*(B2), B02403. https://doi.org/10.1029/2007jb005100
Lagabrielle, Y., Moigne, J. L., Maury, R. C., Cotten, J., & Bourgois, J. (1994). Volcanic record of the subduction of an active spreading ridge, Taitao peninsula (southern Chile). *Geology*, *22*(6), 515. https://doi.org/10.1130/0091-7613(1994)022<0515:vrotso>2.3.co;2
Lagarrigue, S., Veloso, E., Sanhueza, J., Crempien, J., Araya Vargas, J., Suárez, F., & Yáñez, G. (2021). The Chile Ridge Subduction and its influence on the faulting architecture and fluid migration patterns in Patagonia. In *AGU fall meeting, New Orleans, LA and virtual*. Retrieved from https://ui.adsabs.harvard.edu/abs/2021AGUFMDI45D0040L/abstract
Lyakhovsky, V., Shalev, E., Kurzon, I., Zhu, W., Montesi, L., & Shapiro, N. M. (2021). Effective seismic wave velocities and attenuation in partially molten rocks. *Earth and Planetary Science Letters*, *572*, 117117. https://doi.org/10.1016/j.epsl.2021.117117

Madsen, J., Thorkelson, D., Friedman, R., & Marshall, D. (2006). Supplemental material: Cenozoic to recent plate configurations in the Pacific basin: Ridge subduction and slab window magmatism in western North America. https://doi.org/10.1130/geos.s.12237731.v2

Maksymowicz, A., Contreras-Reyes, E., Grevemeyer, I., & Flueh, E. R. (2012). Structure and geodynamics of the post-collision zone between the Nazca–Antarctic spreading center and South America. *Earth and Planetary Science Letters*, *345–348*, 27–37. https://doi.org/10.1016/j.epsl.2012.06.023

Mark, H. F., Wiens, D. A., Ivins, E. R., Richter, A., Ben Mansour, W., Magnani, M. B., et al. (2021). Velocity and viscosity models for southern Patagonia, from the GUANACO experiment [Dataset]. Zenodo. https://doi.org/10.5281/zenodo.5794167

Mark, H. F., Wiens, D. A., Ivins, E. R., Richter, A., Ben Mansour, W., Magnani, M. B., et al. (2022). Lithospheric erosion in the patagonian slab window, and implications for glacial isostasy. *Geophysical Research Letters*, *49*(2), e2021GL096863. https://doi.org/10.1029/2021gl096863

Melnick, D., Bookhagen, B., Strecker, M. R., & Echtler, H. P. (2009). Segmentation of megathrust rupture zones from fore-arc deformation patterns over hundreds to millions of years, Arauco peninsula, Chile. *Journal of Geophysical Research*, *114*(B1), B01407. https://doi.org/10.1029/2008jb005788

Morgan, W. J. (1971). Convection plumes in the lower mantle. *Nature*, *230*(5288), 42–43. https://doi.org/10.1038/230042a0

Murdie, R. E., Pugh, D. T., & Styles, P. (1998). A lightweight, portable, digital probe for measuring the thermal gradient in shallow water sediments, with examples from Patagonia. *Geo-Marine Letters*, *18*(4), 315–320. https://doi.org/10.1007/s003670050085

Navarrete, C., Gianni, G., Massaferro, G., & Butler, K. (2020). The fate of the Farallon slab beneath Patagonia and its links to Cenozoic intraplate magmatism, marine transgressions and topographic uplift. *Earth-Science Reviews*, *210*, 103379. https://doi.org/10.1016/j.earscirev.2020.103379

Negri, A., Daniele, L., Aravena, D., Muñoz, M., Delgado, A., & Morata, D. (2018). Decoding fjord water contribution and geochemical processes in the Aysen thermal springs (Southern Patagonia, Chile). *Journal of Geochemical Exploration*, *185*, 1–13. https://doi.org/10.1016/j.gexplo.2017.10.026

Nelson, E., Forsythe, R., & Arit, I. (1994). Ridge collision tectonics in terrane development. *Journal of South American Earth Sciences*, *7*(3–4), 271–278. https://doi.org/10.1016/0895-9811(94)90013-2

Nelson, E., Forsythe, R., Diemer, J., Alien, M., & Urbina, I. (1993). Taitao ophiolite: A ridge collision ophiolite in the forearc of southern Chile (46°S). *Revista Geológica de Chile*, *2*, 137–166.

Nichols, G. T., Wyllie, P. J., & Stern, C. R. (1994). Subduction zone melting of pelagic sediments constrained by melting experiments. *Nature*, *371*(6500), 785–788. https://doi.org/10.1038/371785a0

Nikolaeva, K., Gerya, T. V., & Connolly, J. A. (2008). Numerical modelling of crustal growth in intraoceanic volcanic arcs. *Physics of the Earth and Planetary Interiors*, *171*(1–4), 336–356. https://doi.org/10.1016/j.pepi.2008.06.026

Olsen, K. M., Bangs, N. L., Tréhu, A. M., Han, S., Arnulf, A., & Contreras-Reyes, E. (2020). Thick, strong sediment subduction along south-central Chile and its role in great earthquakes. *Earth and Planetary Science Letters*, *538*, 116195. https://doi.org/10.1016/j.epsl.2020.116195

Pedoja, K., Regard, V., Husson, L., Martinod, J., Guillaume, B., Fucks, E., et al. (2011). Uplift of quaternary shorelines in eastern Patagonia: Darwin revisited. *Geomorphology*, *127*(3–4), 121–142. https://doi.org/10.1016/j.geomorph.2010.08.003

Phipps Morgan, J., Morgan, W. J., & Price, E. (1995). Hotspot melting generates both hotspot volcanism and a hotspot swell? *Journal of Geophysical Research*, *100*(B5), 8045–8062. https://doi.org/10.1029/94jb02887

Qiuming, C. (2016). Fractal density and Singularity analysis of heat flow over ocean ridges. *Scientific Reports*, *6*(1), 19167. https://doi.org/10.1038/srep19167

Ramos, V. A., & Kay, S. M. (1992). Southern Patagonian plateau basalts and deformation: Backarc testimony of ridge collisions. *Tectonophysics*, *205*(1–3), 261–282. https://doi.org/10.1016/0040-1951(92)90430-e

Ranalli, G. (1995). *Rheology of the earth*. Springer Science & Business Media.

Richter, A., Ivins, E., Lange, H., Mendoza, L., Schröder, L., Hormaechea, J., et al. (2016). Crustal deformation across the southern Patagonian icefield observed by GNSS. *Earth and Planetary Science Letters*, *452*, 206–215. https://doi.org/10.1016/j.epsl.2016.07.042

Russo, R. M., Luo, H., Wang, K., Ambrosius, B., Mocanu, V., He, J., et al. (2022). Lateral variation in slab window viscosity inferred from global navigation satellite system (GNSS)–observed uplift due to recent mass loss at Patagonia ice fields. *Geology*, *50*(1), 111–115. https://doi.org/10.1130/g49388.1

Russo, R. M., VanDecar, J. C., Comte, D., Mocanu, V. I., Gallego, A., & Murdie, R. E. (2010). Subduction of the Chile ridge: Upper mantle structure and flow. *Geological Society of America Today*, *20*, 4–10. https://doi.org/10.1130/gsatg61a.1

Rychert, C., Harmon, N., Constable, S., & Wang, S. (2020). The nature of the lithosphere-asthenosphere boundary. *Journal of Geophysical Research: Solid Earth*, *125*(10), e2018JB016463. https://doi.org/10.1029/2018JB016463

Sanhueza, J., Yáñez, G., Barra, F., Maringue, J., Figueroa, R., & Sáez, E. (2022). Rheological, petrophysical and geometrical constraints of a subduction channel from a numerical model perspective: Insights from la cabana Paleozoic peridotites, coastal cordillera of south-central Chile. *Journal of South American Earth Sciences*, *114*, 103706. https://doi.org/10.1016/j.jsames.2021.103706

Scalabrino, B., Lagabrielle, Y., Rupelle, A. D., Malavieille, J., Polvé, M., Espinoza, F., et al. (2009). Subduction of an active spreading ridge beneath southern South America: A review of the Cenozoic geological records from the Andean foreland, central Patagonia (46–47°s). *Subduction Zone Geodynamics*, 227–246. https://doi.org/10.1007/978-3-540-87974-9_12

Schmeling, H., Babeyko, A., Enns, A., Faccenna, C., Funiciello, F., Gerya, T., et al. (2008). A benchmark comparison of spontaneous subduction models—Towards a free surface. *Physics of the Earth and Planetary Interiors*, *171*(1–4), 198–223. https://doi.org/10.1016/j.pepi.2008.06.028

Seton, M., Flament, N., Whittaker, J., Müller, R. D., Gurnis, M., & Bower, D. J. (2015). Ridge subduction sparked reorganization of the Pacific plate-mantle system 60–50 million years ago. *Geophysical Research Letters*, *42*(6), 1732–1740. https://doi.org/10.1002/2015gl063057

Sisson, V. B., Hollister, L. S., & Onstott, T. C. (1989). Petrologic and age constraints on the origin of a low-pressure/high-temperature metamorphic complex, southern Alaska. *Journal of Geophysical Research*, *94*(B4), 4392–4410. https://doi.org/10.1029/jb094ib04p04392

Sisson, V. B., & Pavlis, T. L. (1993). Geologic consequences of plate reorganization: An example from the Eocene southern Alaska fore arc. *Geology*, *21*(10), 913. https://doi.org/10.1130/0091-7613(1993)021<0913:GCOPRA>2.3.CO;2

Sisson, V. B., Pavlis, T. L., Roeske, S. M., & Thorkelson, D. J. (2003). Introduction: An overview of ridge-trench interactions in modern and ancient settings. In *Special paper 371: Geology of a transpressional orogen developed during ridge-trench interaction along the North pacific margin* (pp. 1–18). https://doi.org/10.1130/0-8137-2371-x.1

Spiegelman, M., & McKenzie, D. (1987). Simple 2-D models for melt extraction at mid-ocean ridges and island arcs. *Earth and Planetary Science Letters*, *83*(1–4), 137–152. https://doi.org/10.1016/0012-821x(87)90057-4

Stein, C. A., & Stein, S. (1992). A model for the global variation in oceanic depth and heat flow with lithospheric age. *Nature*, *359*(6391), 123–129. https://doi.org/10.1038/359123a0

Stein, C. A., Stein, S., & Pelayo, A. M. (1995). Heat flow and hydrothermal circulation. Seafloor hydrothermal systems: Physical, chemical, biological, and geological interactions. *Geophysical Monograph*, *91*, 425–445. https://doi.org/10.1029/gm091p0425

Stern, C. R., & Kilian, R. (1996). Role of the subducted slab, mantle wedge and continental crust in the generation of adakites from the Andean Austral volcanic zone. *Contributions to Mineralogy and Petrology*, *123*(3), 263–281. https://doi.org/10.1007/s004100050155
Stern, R. J. (2002). Subduction zones. *Reviews of Geophysics*, *40*(4), 3-1–3-38. https://doi.org/10.1029/2001rg000108
Stixrude, L., & Lithgow-Bertelloni, C. (2011). Thermodynamics of mantle minerals—I. Phase equilibria. *Geophysical Journal International*, *184*(3), 1180–1213. https://doi.org/10.1111/j.1365-246x.2010.04890.x
Suárez, R., Sue, C., Ghiglione, M., Guillaume, B., Ramos, M., Martinod, J., & Barberón, V. (2021). Seismotectonic implications of the south Chile ridge subduction beneath the Patagonian Andes. *Terra Nova*, *33*(4), 364–374. https://doi.org/10.1111/ter.12521
Tebbens, S. F., & Cande, S. C. (1997). Southeast Pacific tectonic evolution from early Oligocene to present. *Journal of Geophysical Research*, *102*(B6), 12061–12084. https://doi.org/10.1029/96jb02582
Tebbens, S. F., Cande, S. C., Kovacs, L., Parra, J. C., LaBrecque, J. L., & Vergara, H. (1997). The Chile ridge: A tectonic framework. *Journal of Geophysical Research*, *102*(B6), 12035–12059. https://doi.org/10.1029/96jb02581
Thomson, S. N., Brandon, M. T., Tomkin, J. H., Reiners, P. W., Vásquez, C., & Wilson, N. J. (2010). Glaciation as a destructive and constructive control on mountain building. *Nature*, *467*(7313), 313–317. https://doi.org/10.1038/nature09365
Thorkelson, D. J. (1996). Subduction of diverging plates and the principles of slab window formation. *Tectonophysics*, *255*(1–2), 47–63. https://doi.org/10.1016/0040-1951(95)00106-9
Thorkelson, D. J., & Taylor, R. P. (1989). Cordilleran slab windows. *Geology*, *17*(9), 833. https://doi.org/10.1130/0091-7613(1989)017<0833:csw>2.3.co;2
Turcotte, D. L., & Schubert, G. (2014). *Geodynamics*. Cambridge University Press.
Uyeda, S., & Miyashiro, A. (1974). Plate tectonics and the Japanese islands: A synthesis. *Geological Society of America Bulletin*, *85*(7), 1159–1170. https://doi.org/10.1130/0016-7606(1974)85<1159:ptatji>2.0.co;2
Veloso, E. A., Anma, R., & Yamazaki, T. (2005). Tectonic rotations during the Chile ridge collision and obduction of the Taitao ophiolite (southern Chile). *Island Arc*, *14*(4), 599–615. https://doi.org/10.1111/j.1440-1738.2005.00487.x
Villar-Muñoz, L., Behrmann, J. H., Diaz-Naveas, J., Klaeschen, D., & Karstens, J. (2013). Heat flow in the southern Chile forearc controlled by large-scale tectonic processes. *Geo-Marine Letters*, *34*(2–3), 185–198. https://doi.org/10.1007/s00367-013-0353-z
Villar-Muñoz, L., Kinoshita, M., Bento, J. P., Vargas-Cordero, I., Contreras-Reyes, E., Tinivella, U., et al. (2021). A cold seep triggered by a hot ridge subduction. *Scientific Reports*, *11*(1), 20923. https://doi.org/10.1038/s41598-021-00414-3
Wu, Y., Liao, J., Guo, F., Wang, X. C., & Shen, Y. (2022). Styles of Trench-Parallel mid-ocean ridge subduction affect Cenozoic geological evolution in Circum-Pacific continental margins. *Geophysical Research Letters*, *49*(8), e2022GL098428. https://doi.org/10.1029/2022gl098428
Yáñez, G., & Cembrano, J. (2004). Role of viscous plate coupling in the late tertiary Andean tectonics. *Journal of Geophysical Research*, *109*(B2), B02407. https://doi.org/10.1029/2003jb002494
Zhao, G. (2014). Paleoproterozoic Amalgamation of the North China Craton. In *Precambrian evolution of the North China Craton* (pp. 95–147). https://doi.org/10.1016/b978-0-12-407227-5.00004-3

References From the Supporting Information

Clauser, C., & Huenges, E. (1995). Thermal conductivity of rocks and minerals. In T. J. Ahrens (Ed.), *Rock physics & phase relations: A handbook of physical constants* (pp. 105–126).
Connolly, J. A. (2005). Computation of phase equilibria by linear programming: A tool for geodynamic modeling and its application to subduction zone decarbonation. *Earth and Planetary Science Letters*, *236*(1–2), 524–541. https://doi.org/10.1016/j.epsl.2005.04.033
Connolly, J. A. (2009). The geodynamic equation of state: What and how. *Geochemistry, Geophysics, Geosystems*, *10*(10), 30. https://doi.org/10.1029/2009gc002540
Connolly, J. A., & Kerrick, D. (2002). Metamorphic controls on seismic velocity of subducted oceanic crust at 100–250 km depth. *Earth and Planetary Science Letters*, *204*(1–2), 61–74. https://doi.org/10.1016/s0012-821x(02)00957-3
Gerya, T. V., & Meilick, F. I. (2010). Geodynamic regimes of subduction under an active margin: Effects of rheological weakening by fluids and melts. *Journal of Metamorphic Geology*, *29*(1), 7–31. https://doi.org/10.1111/j.1525-1314.2010.00904.x
Gerya, T. V., Stern, R. J., Baes, M., Sobolev, S. V., & Whattam, S. A. (2015). Plate tectonics on the earth triggered by plume-induced subduction initiation. *Nature*, *527*(7577), 221–225. https://doi.org/10.1038/nature15752
Gorczyk, W., Willner, A. P., Gerya, T. V., Connolly, J. A., & Burg, J. (2007). Physical controls of magmatic productivity at Pacific-type convergent margins: Numerical modelling. *Physics of the Earth and Planetary Interiors*, *163*(1–4), 209–232. https://doi.org/10.1016/j.pepi.2007.05.010
Hart, S. R., & Zindler, A. (1986). In search of a bulk-earth composition. *Chemical Geology*, *57*(3–4), 247–267. https://doi.org/10.1016/0009-2541(86)90053-7
Matthews, K. J., Maloney, K. T., Zahirovic, S., Williams, S. E., Seton, M., & Müller, R. D. (2016). Global plate boundary evolution and kinematics since the late Paleozoic. *Global and Planetary Change*, *146*, 226–250. https://doi.org/10.1016/j.gloplacha.2016.10.002
Stixrude, L., & Lithgow-Bertelloni, C. (2005). Thermodynamics of mantle minerals—I. Physical properties. *Geophysical Journal International*, *162*(2), 610–632. https://doi.org/10.1111/j.1365-246x.2005.02642.x
Zunino, A., Connolly, J. A., & Khan, A. (2011). Precalculated phase equilibrium models for geophysical properties of the crust and mantle as a function of composition. *Geochemistry, Geophysics, Geosystems*, *12*(4), Q04001. https://doi.org/10.1029/2010gc003304